5-4-2022

Effects of Urban Land Cover on Magnitude and Interannual Variability of Evapotranspiration

Dinah K. Carlton
Georgia State University

Effects of Urban Land Cover on Magnitude and Interannual Variability of Evapotranspiration

by

Dinah Carlton

Under the Direction of Luke Pangle, PhD and Jeremy Diem, PhD

A Thesis Submitted in Partial Fulfillment of the Requirements for the Degree of

Master of Science

in the College of Arts and Sciences

Georgia State University

2022

ABSTRACT

Quantifying actual evapotranspiration (AET) in urbanized watersheds helps water managers develop accurate water budgets and aids in predicting future water budgets, especially in the face of land-cover and climate change. This paper presents multiple methods, with focus on Penman-Monteith approach, to estimate 20 years of daily, monthly, and annual AET totals in an urbanized watershed, the South River watershed (SRW), in Atlanta, GA. Land cover analysis confirmed NLCD definitions and revealed developed classes 21-24 contain 48.18%, 24.26%, 13.79%, and 4.43% forest cover, respectively. Additionally, it was found that the annual AET of the SRW is approximately 800 mm/yr, with about 10% of coming solely from impervious land cover. A decreasing annual AET trend was observed for the SRW, resulting from land cover changes and decreasing incoming solar radiation. Finally, TerraClimate reference ET datasets overestimated urban ET, while statistical models typically underestimated ET when compared to reference water balance ET estimates.

INDEX WORDS: Evapotranspiration, Penman-Monteith, Urban, Land cover, Hydrology, Water budget, Heterogeneous

Effects of Urban Landcover on Magnitude and Interannual Variability of Evapotranspiration

by

Dinah Carlton

Committee Chairs: Luke Pangle, Jeremy Diem

Committee: Luke Pangle

Jeremy Diem

Sarah Ledford

Electronic Version Approved:

Office of Graduate Services

College of Arts and Sciences

Georgia State University

May 2022

ACKNOWLEDGEMENTS

I would like to acknowledge the efforts of so many that helped and guided me throughout my master's program at Georgia State University. Firstly, I would like to thank my committee chairs Dr. Luke Pangle and Dr. Jeremy Diem for their support and guidance in research urban evapotranspiration. The help from Dr. Jeremy Diem was unmatched when it came to my questions with quick responses and considerable desire to promptly investigate said questions. Dr. Luke Pangle served as an intelligent sounding board for ideas and gave educated insight on many concepts and calculations throughout my research. I would also like to thank the last member of my thesis committee Dr. Sarah H. Ledford for her support with both educational and mental challenges I faced during my time at GSU. Finally, my research could not have been completed without the technical support of my fiancé and fellow graduate student at the University of Georgia, Caleb Sytsma. His knowledge of R coding aided me to get to the results presented in this thesis.

TABLE OF CONTENTS

LIST OF TABLES

LIST OF FIGURES

1 INTRODUCTION

Urban watersheds are composed of a more complex array of landscape elements when compared to rural watersheds. The heterogeneous composition of greenspace, buildings, and other impervious surfaces can make quantifying environmental processes much more difficult (Abdullah et al., 2019). New structural additions can be observed in urban environments like extensive pipe networks, water treatment/sewer treatment facilities, and built surfaces (Collier & Venables, 2016). The urban landscape can be compared to a forest, where the space between buildings and trees is considered to be the 'urban canopy' (Grimmond & Oke, 1991). These spaces are called street canyons, where the height of buildings and resulting size of street canyons impact atmospheric processes like wind flow regimes and wind speeds (Kastner-Klein et al., 2004; Xie et al., 2005). Hydrologic processes are altered as percent cover of impervious surface increases (McMahon et al., 2003), where total runoff is drastically increased, infiltration is decreased (Hollis, 1988; McMahon et al., 2003; J. D. Miller et al., 2014), and precipitation frequency and intensity are increased (Changnon et al., 1971; Diem, 2007; J. Liu & Niyogi, 2019). While the main driver of altered hydrology is percent imperviousness, urban lands also introduce new methods of water movement like anthropogenic-induced inter-basin transfers, pipe systems leaking into groundwater supplies, and increased water inputs by residential/commercial irrigation (Bhaskar, Beesley, et al., 2016; Bhaskar, Hogan, et al., 2016; Hopkins et al., 2015; Kaushal & Belt, 2012; Kokkonen et al., 2018).

Heterogeneous land cover coupled with additional water inputs, reservoirs, and outputs can complicate quantifying components of an urban water budget, especially evapotranspiration. Actual evapotranspiration, or AET, is defined as the combination of evaporative transfer of water from open water and transpiration through plant stomata as vapor (Thornthwaite, 1948), where

about 97% of terrestrial AET is from land surfaces and the remaining 3% is from open water (Dingman, 2002). This is a paramount hydrologic process in most watersheds, accounting for as much as 65% of precipitation that falls across global landmasses (Healy et al., 2007). Potential ET, PET, can be conceptualized as a reference quantity of water transfer most used for estimating agricultural crop water demand that is representative of the ET magnitude when water in the environment is not limited (Eagleman, 1967; Thornthwaite, 1948). Total AET is positively correlated with temperature, net solar radiation, wind speed, but negatively correlated with relative humidity (Y. Fang et al., 2016a; Hamilton et al., 2018; Hao et al., 2018; Hogan et al., 2020; Thompson et al., 2011; Williams et al., 2012). In humid regions, AET is thought to decrease in urban areas due to less vegetative cover and decreased soil moisture (Bhaskar & Welty, 2012; Fang et al., 2020; Peters et al., 2011); however, in some suburban areas in summer dry climates, AET is observed to increase and create an "oasis" effect because of larger lot sizes, more automated irrigation systems, and better-maintained lawns and gardens (Kokkonen et al., 2018; Oke, 1979). Urban irrigation also leads to seasonal patterns of higher AET in the spring and summer months (Grimmond & Oke, 1986; Kokkonen et al., 2018), and can even surpass AET rates of local forested regions (Claessens et al., 2006). Decreased AET in urban areas can also lead to an effect called the urban dry island (UDI), where urbanization is related to greater vapor pressure deficits and lower overall relative humidity when compared to nearby rural areas, particularly in humid regions (Hao et al., 2018).

Urban areas alter many meteorological processes that influence AET rates and magnitudes. While there can be distinct temperature variability in proximate areas because of heterogeneous land cover, on average cities can be 1-3^{o}C warmer than their rural counterparts, and as much as 12^{o}C difference has been observed in some locations (Oke, 1981). This is called the urban heat

island (UHI), and Oke (1981) found that the magnitude of temperature increase is proportional to city size. Percent of impervious cover accounts for most of the land surface temperature variation, which indicates that percent impervious cover can be a good indicator of the urban heat island effect (F. Yuan & Bauer, 2007). Urbanized areas also display lower albedo, or the fraction of radiative energy reflected from the land surface, as a result of decreased vegetative cover and increased impervious cover, leading to higher surface temperatures that radiate into the atmosphere and further increase air temperatures (Trlica et al., 2017). Urban building density also affects the amount of solar radiation certain areas receive because of structural shading (Hwang et al., 2011), impacting the growth of vegetation and ecosystem water use.

Based on the reviewed body of literature, AET in urban areas generally remains a complicated and challenging process to quantify for many reasons. Accurate estimates of urban AET are dependent on scale of analysis (Aminzadeh & Or, 2017; Famiglietti & Wood, 1995) Famiglietti & Wood (1995) showed how representative areas contributing to AET with in a catchment vary throughout the day and that dominant processes controlling AET vary with scale of analysis. The scale of analysis and degree of heterogeneity also effect the atmospheric dynamics of the convective boundary layer, altering spatial AET patterns (Aminzadeh & Or, 2017). Accuracy of AET estimates also depended on methods used (Fisher et al., 2011; Gao et al., 2020; Zhang et al., 2001). Commonly used AET models such as the Thornthwaite approach, Priestley–Taylor approach, and the Penman–Monteith can differ by as much as 7%-30% from local eddy covariance towers (Fisher et al., 2011). Additionally, it is difficult to adequately quantify competing processes that individually have different effects on overall AET rates and magnitude. One account indicated that climate change increased AET by 29% due to higher temperatures, an increase in precipitation, and a decrease in relative humidity, whereas land

cover change decreased AET by 50 % due to conversion of vegetated cover to urban developments (Fang et al., 2020), leading to an overall decrease in AET over the study period. Finally, there still currently seems to be no consensus in scientific literature as to which methods are preferred in estimating urban AET because studies tend to use the method that corresponds to the data available (Fisher et al., 2011).

Historically, many methods to estimate AET have been documented. The most accurate way to directly measure AET remains to be through eddy covariance towers (Scott, 2010). This approach uses sensors placed on towers of various heights to measure the turbulent exchange of carbon dioxide along with latent and sensible heat fluxes in the atmosphere (Baldocchi et al., 2000, 2001). Direct AET measurements using traditional towers are expensive and in turn limits the utility of this method (Hill et al., 2017). It can be also be challenging to interpret measurements in regions where the tower footprint includes heterogeneous land cover types, and until recently, determining the actual footprint of a tower has been difficult (Barcza et al., 2009; Göckede et al., 2004). The most common method to estimate AET is through a water balance approach in watersheds with minimal anthropogenic modification, where AET is interpreted as a residual with all other terms quantified in a closed system. This is a theoretically simple equation that incorporates inflows and outflows of a watershed, but the resulting estimates of AET depend on the accuracy of the other quantified terms and should not be used when the goal is to achieve water balance closure (Brutsaert, 2005). The accuracy of this method increases as the length of temporal resolution increases due to decreasing error in changes in storage (Dingman, 2002). When eddy covariance towers and water balance approaches are not possible, the most common way to model AET is Penman-Monteith approach because of its ability to represent physically-based surface characteristics (Allen et al., 1998; Diouf et al., 2016). This equation’s form was

created as an adaptation to Penman's equation for evaporation to include vegetation transpiration, and it requires meteorological data of monthly, daily, or hourly temperature, humidity, solar radiation, and wind speed (Monteith, 1965). There is significant precedent of implementing the Penman-Monteith equation by dividing heterogeneous landcovers into homogeneous sub-areas that can be aggregated to areal AET totals (Choi et al., 2012; Grimmond & Oke, 1991; Hao et al., 2018; Jia et al., 2001; Kokkonen et al., 2018; Raoufi & Beighley, 2017; Stewart, 1989; J. Wang et al., 2008).

The long-term interannual variability of AET in increasingly urban areas remains unclear. Literature shows that interannual patterns of AET are relatively unchanged from year to year in vegetated regions as a result of little land cover change, deep water storage, vegetation roots' ability to access water without precipitation events (B. Fang et al., 2020; Fatichi & Ivanov, 2014; Hamilton et al., 2018; Oishi et al., 2010). In one recent long-term study, a decreasing AET trend of an average of 1.35 mm/year is observed because of land cover change in urban and suburban areas; however, this decrease is somewhat offset by residential irrigation (Kokkonen et al., 2018). While it is known that annual AET is generally reduced in urban areas due to less vegetative cover and lower soil moisture (Bhaskar & Welty, 2012; B. Fang et al., 2020; Peters et al., 2011), still, little is understood about the interannual variability of urban AET.

Even considering the known challenges in estimating urban AET, it is now more important than ever to understand urban AET patterns and rectify some uncertainties in AET estimation methods. As global urban populations increase and urban temperatures continue to increase, it is also important to understand the implications of urban sprawl. Much like humans sweat to cool their bodies, the land surface can be cooled through AET of water vapor from vegetation into the atmosphere (C. Tan et al., 2015). This fact suggests there may be increasing utility in using AET

as a tool for reducing urban terrestrial and air temperatures; however, knowledge must be acquired about baseline urban AET trends. Reducing urban temperatures can help fight heat related illnesses and, in extreme cases, even death (J. Tan et al., 2010). Illuminating the interannual variability, or invariability, of urban AET and how it shifts with respect to land cover change will aid water resource managers in predicting future watershed water demands and give city planners some supporting evidence for the need of green infrastructure development. The objectives of this study are as follows: 1) conduct a detailed land cover analysis to analyze the composition of developed NLCD classes, 2) quantify long-term AET estimates using the Penman-Monteith approach and analyze the interannual variability of AET with respect to changes in land cover and atmospheric conditions, and 3) compare Penman-Monteith estimates to estimates of actual evapotranspiration from both statistical models and publicly-available gridded datasets.

1.1 Study Area

This study takes place in the South River watershed, SRW, which is located in the Atlanta, Georgia USA metropolitan area and is an ideal study area for an analysis of the interannual variability of AET in an urban watershed (Figure 1). The study area encompasses parts of five different counties in Georgia: Fulton County, DeKalb County, Clayton County, Henry County, and Rockdale County. The SRW is located entirely within the Piedmont physiographical region that consists of underlying structures of crystalline metamorphic rocks, like gneiss and schist, and igneous rocks, like granite (J. Miller, 1990). The Piedmont region receives between 1143-1524 mm of annual precipitation that is evenly distributed throughout the year and experiences on average 230 freeze-free days (NRCS Georgia, 2020). The humid subtropical climate supports many types of vegetation with increasing growing season lengths and can be observed in many

locales across the globe (Belda et al., 2014; Xia et al., 2013), making the results of this study useful for urban and urbanizing areas in many countries. Additionally, the Georgia Environmental Monitoring Network (GAEMN) operates a vast system of dispersed, long-term weather stations across the state that measure data at sub-daily timescales, allowing for continuous daily calculations since the beginning of the study period. The study period, January 2001- December 2020, was chosen because detailed land cover data are available throughout and twenty years of continuous AET estimates can help predict hydrologic conditions for the next two critical decades in climate change progression.

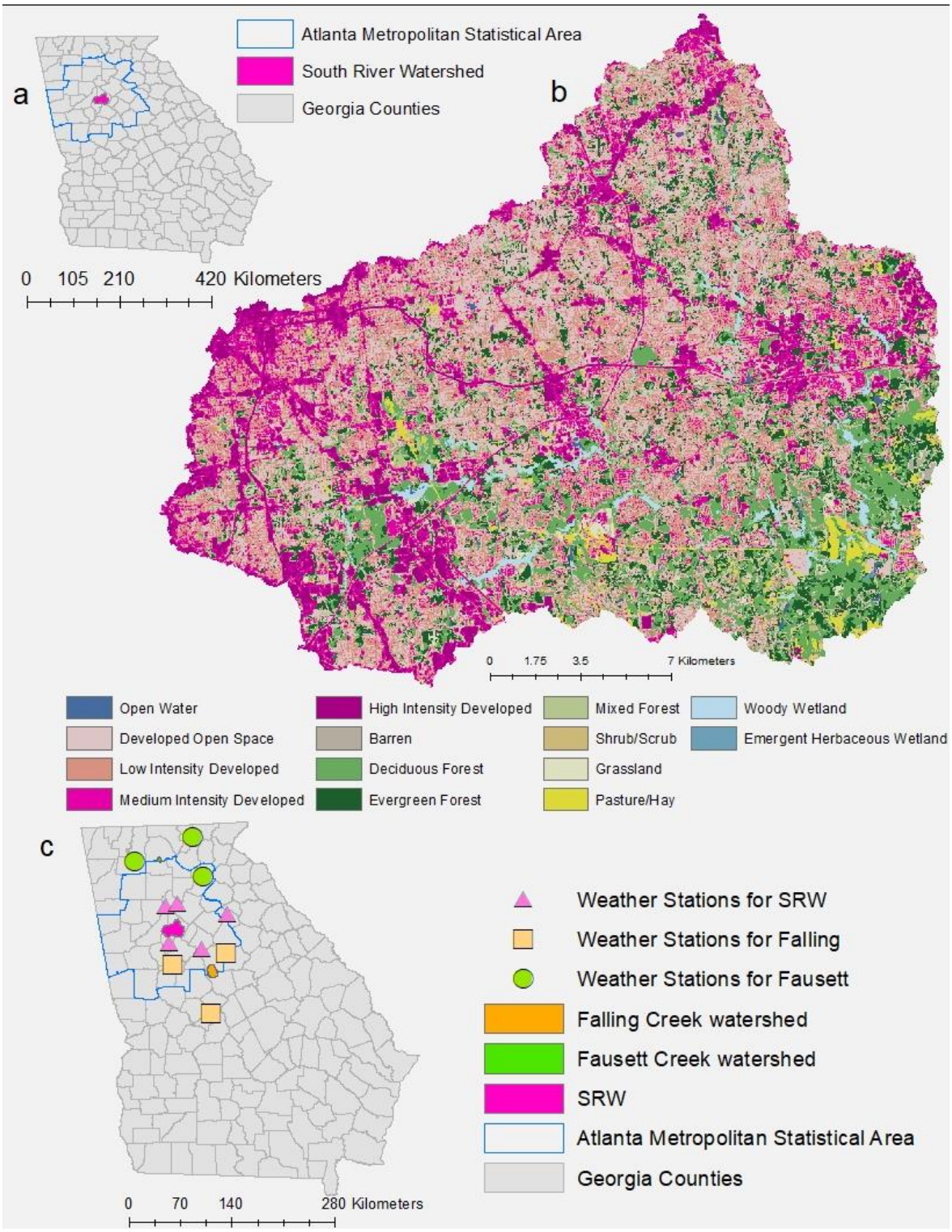

Figure 1: (a) The state of Georgia, United States, light gray, with county boundaries, dark gray, and South River watershed boundary, pink; (b) South River watershed with 14 NLCD land cover classes; (c) South River watershed with reference watersheds, Falling Creek and Fausett Creek, and each of their respective GAEMN weather stations.

2 METHODS

2.1 Synopsis of Meteorological Trends

To make interpreting AET results easier, meteorological conditions should be analyzed for any possible trends since 2001. This step is imperative to understanding AET, as AET is driven by a multitude of meteorological inputs. The most pertinent variables to analyze included temperature, precipitation, incoming solar radiation, and vapor pressure deficit. Trends in meteorological trends over 2001-2020 were assessed using Kendall-Tau correlation tests (α= 0.05; one-tailed). Changes in temperature alter net radiation, vapor pressure, and latent heat of vaporization. Incoming solar radiation alters the net radiation observed and surface resistance. Precipitation alters the runoff and storage in each surface type affecting AET, especially in impervious land cover classes. Finally, the vapor pressure deficit is a direct variable in the PM equation. The specifics of all PM variables are described in section 2.3. In all, understanding the climatic conditions and trends within the SRW can illuminate reasons for any AET trends that might be observed.

2.2 Land Cover Analysis

Land-cover data sets created in 2019 were obtained from USGS National Land Cover Database (NLCD) to complete a more detailed analysis of land-cover in classes that may not be as specific as needed, such as “developed open space”, “low-intensity developed”, “medium-intensity developed”, and “high-intensity developed”. Land-cover classes such as these are not descriptive enough to accurately quantify AET, as formulas require specific land-cover parameter details, like storage capacity, feature heights, surface albedo, and many more, as depicted in Table 2. Each land cover class in the South River Watershed study area was extracted in ESRI ArcMap and converted to a polygon. Following layer extraction, 30 random points were

created in each developed land cover class (Figure 2), and point data sets were exported as a '.kml' file to use in Google Earth Pro. A 10 m fishnet was imported as well to aid land cover analysis. Using the fishnet, each point location was visited in Google Earth Pro and served as the center of a 3x3 grid area where the actual land cover was recorded, meaning each developed land cover class was analyzed using 270 total points. We used this fishnet method and number of points analyzed to address the increasingly heterogeneous nature of developed land cover. Alternatively, 50 random points were created in undeveloped land cover classes at which only the land cover at the direct point was recorded (Figure 2). A total of 50 points are used to analyze the composition of each undeveloped class. In each land cover class, the number of each land cover code was counted to get percentages of cover which was then multiplied by the area of the original land cover class area. Forest cover in all classes, except for forest cover in the deciduous forest class and the conifer forest class, were assumed to be "mixed forest". Forest cover in the deciduous and conifer forest classes were assumed to be the forest type of their respective classes. An example of this procedure is shown in Figure 3 and Table 1.

The USGS National Land Cover Database (NLCD) could only provide land cover data from the years 2001, 2004, 2006, 2008, 2011, 2013, 2016, and 2019. The Kendall-Theil robust line, the median of the slopes between all combinations of two points of actual area of each class in the data (Helsel & Hirsch, 2002), was used to estimate annual values for all 20 years. After recording and consolidating land use and land cover data, the resulting landcover classes are open water, impervious areas, grassland, shrubland, forest, wetland/marsh. Interpolation and extrapolation of eight years of landcover information from the National Land Cover Database (NLCD) with an examination of 2019 data in conjunction with Google Earth imagery enabled a detailed landcover database to be constructed over 2001-2020.

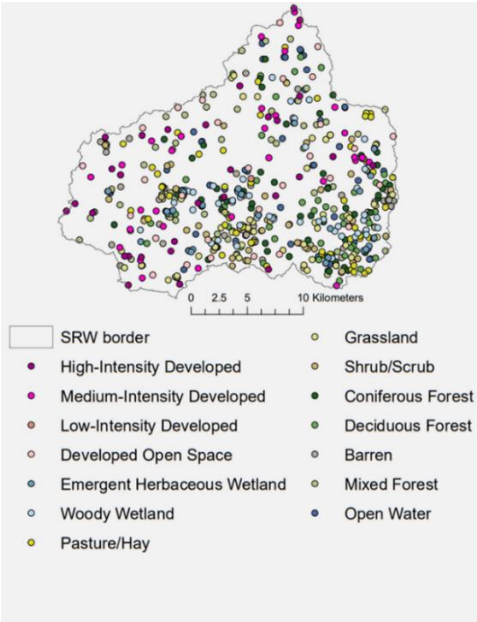

Figure 2: Locations and spatial distribution of the spatial sampling sites within each NLCD land cover class in the SRW.

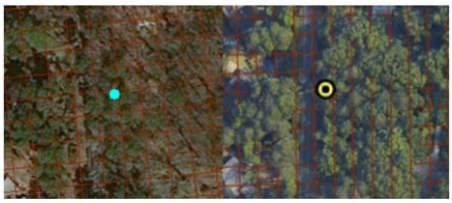

Figure 3: Example of landcover perception in ArcGIS using the default base map (left) and Google Earth Pro (right) using point data sets and a 10 m fishnet (red grid lines). This is 'point 1' of USGS NLCD land cover class 21, developed open space.

Table 1: Example of 'point 1' landcover 3x3 grid using Google Earth Pro and recorded in Microsoft Word tables, where 1= forest and 2= paved roads (later combined with others and called 'impervious').

1		
2	1	1
2	1	1
2	1	1

2.3 Penman-Monteith Method

AET will be estimated using the Penman-Monteith (PM) approach. The updated PM equation for urban areas requires data of net solar radiation, anthropogenic heat flux, storage heat flux, vapor pressure deficit, aerodynamic resistance, surface resistance, the specific heat of air,

and the psychometric constant (Grimmond & Oke, 1991). This equation is a combination model, incorporating atmospheric and surface-specific information, and is recommended by the Food and Agriculture Organization (FAO) of the United Nations. This approach is useful because it incorporates equations and parameters to explicitly represent how different surface types influence net radiation, aerodynamic resistance, and surface resistance terms. The PM equation addresses that AET is not only affected by atmospheric conditions, like net solar radiation and vapor-pressure deficit, but also by the unique properties of surfaces and biological processes of plants in the aerodynamic and surface resistance parameters. The PM equation is chosen for use in this study because there is increased confidence in final estimates due to the incorporation all the environmental parameters that impact AET processes across any land cover type like temperature, solar radiation, humidity, and wind speed. Additionally, because the PM equation returns chronologically continuous AET estimates and it has been shown to agree with some water balance estimates (Mao & Wang, 2017), we can use this method to analyze the interannual variability of AET. Regression models described in later sections only produce long-term estimates.

The PM equation is only one stage of the procedure needed to create AET estimates in urban areas. Because the amount of AET varies considerably with surface type, a detailed land cover analysis is conducted to determine the actual land cover of the South River watershed, as detailed in section 2.2. The PM equation returns an estimate for each land cover class that describes the AET if the whole study area was that respective land cover, so the land cover areas determined by the analysis procedures are framed as proportions of total areas and multiplied by the respective AET estimate to scale AET accordingly. After AET estimates are scaled to the proportion of land cover in the study area, a running canopy storage model is implemented to

address the water availability in each land cover type. Accounting for surface water availability is a procedure that is impactful only on the impervious land cover AET because accounting for runoff in urban areas is imperative to getting the most accurate AET estimates. As the PM equation does not require any water input data, the estimates are technically a potential ET estimate. By using a procedure in Grimmond and Oke (1991), the study can accurately determine if the water available in each land cover type would support the AET modeled by the PM equation, and therefore adjusted accordingly if the water available is not sufficient to support AET. The surface water availability model is detailed in section 2.4. The interannual variability of PM AET is assessed over 2001-2020 using Kendall-Tau correlation tests ($\alpha = 0.05$; one-tailed).

Data required for the Penman-Monteith equation were obtained from multiple sources. Daily meteorological data from January 1, 2001 to December 31, 2020 were obtained from eleven weather stations within GA Environmental Monitoring Network, GAEMN. Regarding the SRW, the five stations used include Covington, Jonesboro, Duluth, Dunwoody, and Watkinsville (UGA). Reference watersheds' stations include Byron, Griffin, and Eatonton for Falling Creek watershed, and Calhoun, Blairsville, and Gainesville for Fausett Creek watershed. Data acquired for the Penman-Monteith method included temperature, total incoming solar radiation, wind speed, relative humidity, and atmospheric pressure. For each meteorologic variable, the average of the available stations was used in most calculations. The Covington station was not active until mid-2002, and some stations had minimal missing data throughout the study period, resulting in an average of only four stations in some intervals. Elevation and latitude were obtained from Google Earth Pro. Land cover specific constants and pertinent submodels were obtained from a multitude of published literature sources and are described hereafter when they

are required. Given that the PM model is the most physically intensive AET model, and all models show some limitations, the estimation of urban evapotranspiration is solved as seen in Grimmond and Oke (1991):

$$Q_E = \frac{s(Q^* + Q_F - \Delta Q_S) + (C_a V)/r_a}{s + \gamma(1 + \frac{r_s}{r_a})} \quad (1)$$

where s is the slope of the saturation vapor pressure versus temperature curve (Pa/^{o}C), R_n is net radiation (W/m^2), Q_F is the anthropogenic heat flux (W/m^2), ΔQ_s is storage heat flux (W/m^2), C_a is heat capacity of air (J/m$^3{}^o$C), V is the vapor pressure deficit (Pa), γ is the psychometric constant (Pa/^{o}C), and r_a and r_s are aerodynamic resistance (s/m) and surface resistance (s/m), respectively. The output of this equation is given as a quantity of energy, not a depth of AET that the study requires. A complete PM AET procedure with conversion procedure using dimensional analysis with the latent heat of vaporization is shown in Figure 4, and a table of all data required for the whole process can be found in Table 6.

Many of the parameters in the PM equation are land cover specific, meaning that each land cover class will have a differing value in their respective calculations. Net radiation is landcover specific because of the variability in surface albedo. Each surface type (i.e.., forest versus impervious) will reflect and absorb solar radiation differently, allowing for variation in how much energy is released back into the atmosphere. The dynamic net radiation variables along with landcover specific constants in the objective hysteresis model used from Grimmond and Oke (1999) also result in land cover specific storage heat flux. As storage heat flux is a measure of how surfaces retain energy, it is intuitive to understand that different surfaces will mediate heat transfer differently. Additionally, aerodynamic resistance will change based on landcover because of the variability in feature height in each class. Surface resistance will be landcover specific because of the dependence on the net radiation in the chosen model and

possibly from irrigation on certain landcover classes, as surface resistance can be impacted by antecedent surface wetness conditions. Finally, anthropogenic heat flux will be landcover specific because of the differences in population densities in each class, but we assume in this study that only developed land cover classes exhibit anthropogenic heat fluxes.

Finally, a sensitivity analysis was conducted to assess how error in input parameters propagates through AET calculation within four different land covers: grass, mixed forest, low-intensity developed, and high-intensity developed. The variables temperature, albedo, feature height, incoming solar radiation, wind speed, and relative humidity were assessed by independently increasing each by 10% or decreasing each by 10%.

Table 2: Coefficients and land-cover specific variables for the Penman-Monteith model and subsequent submodels compiled from a variety of sources. The dashes are instances where the data is not needed or applicable to the specified land cover.

					Storage Heat Flux Coefficients				
	Area (km^2)	Population	Population Density (P/km^2)	Albedo	a1	a2 (h)	a3 (W/m)	Mean height of buildings (m)	Mean height of vegetation (m)
Impervious	113.36	468,481	4132.68						
DOS	8.43	—	475	0.16[a]	0.7	0.33	-38	8.69	—
LID	42.49	—	1413	0.18[a]	0.7	0.33	-38	8.90	—
MID	35.10	—	2777	0.12[a]	0.7	0.33	-38	11.34	—
HID	24.73	—	4118	0.2[a]	0.7	0.33	-38	10.30	—
Forest	210.65								
Deciduous	48.34	0	0	0.136[b]	0.11	0.11	-12.3	—	24.04
Coniferous	43.08	0	0	0.123[b]	0.11	0.11	-12.3	—	27.71
Mixed	119.22	0	0	0.1295[b]	0.11	0.11	-12.3	—	23.15
Grassland	135.78	0	0	0.144[b]	0.34	0.31	-31	—	0.12
Short Vegetation	1.86	0	0	0.156[c]	0.34	0.31	-31	—	3.99
Wetland	5.71	0	0	0.124[b]	0.11	0.11	-12.3	—	8.84
Open water	6.29	0	0	0.0238[b]	0.5	0.21	-39.1	—	0

[a] Stathopoulou et al. (2007)
[b] Brest (1987)
[c] Barnes and Roy (2010)

2.3.1 s, Slope of Vapor Pressure vs Temperature Curve

The slope of the vapor pressure-temperature curve is a variable that shows how saturation vapor pressure of air increases exponentially with increases in temperature. As air temperature rises, the water molecule storage capacity rises, creating higher saturation vapor pressures. The slope of the curve helps describe the process of vaporization, therefor an important parameter to include in the Penman-Monteith equation. It is dependent of surface temperature but can be closely approximated by using air temperature (Raupach, 2001). The equation used is the derivative of the equation used to quantify vapor pressure and is found as:

$$s = \frac{2508.3}{(T+237.3)^2} * exp\frac{(17.3*T)}{T+237.3)} \quad (2)$$

where *T* is temperature (^{o}C). This temperature data was obtained from the average of the five weather stations around the South River watershed. Resulting units are in kPa/K. Conversions may be required to input into the Penman-Monteith equation.

2.3.2 R_n, Net Radiation

Solar radiation is one of the main factors influencing the rate and magnitude of evapotranspiration. The sun's energy physically heats up the atmosphere which transmits energy to plants, increasing the transpiration rate from vegetation. The intensity of this energy is dependent upon the location, time of year, and degree of cloudiness. In the Penman-Monteith approach, the larger term ($R_n + Q_F - \Delta Q_s$) represents the total available energy for AET (Mitchell et al., 2008), so each quantity is important to include in the model's calculations. R_n stands for net radiation, which is defined as the combination of absorption and reflection of both short- and long-wave radiation. It can be quantified as the following equation:

$$R_n = (1-\alpha)R_{si} - L\uparrow + L\downarrow \quad (3)$$

where α is the land surface albedo, Rsi is the incoming solar radiation (W/m^2), L↑ is outgoing longwave radiation (W/m^2), and L↓ is incoming longwave radiation (W/m^2). Because only total incoming solar radiation is provided by the GAEMN, An et al. (2017) gives a procedure for calculating daily net radiation from a few parameters. The equation is as follows:

$$R_n = (1-\alpha)R_{si} - \left[a_c\left(\frac{R_{si}}{R_{so}}\right) + b_c\right]\left(a_1 + b_1 e_d^{0.5}\right)\sigma\left(\frac{T_{avg}^4}{2}\right) \quad (4)$$

where α is land surface albedo, R_{si} is incoming solar radiation (MJ/m^2), a_c and b_c are cloud factors, a_1 and b_1 are emissivity factors, R_{so} is clear sky solar radiation (MJ/m^2), e_d is saturation vapor pressure (kPa), σ is the Stefan-Boltzmann constant (5.67 x 10^{-8} W/m^{2}K^4), and T_{avg} is the average air temperature in K. Albedo data of a variety of surfaces were obtained from Stathopoulou et al. (2007) for impervious cover, Barnes and Roy (2010) for grassland, wetland, short vegetation, open water, and the three types of forest classes. The cloud factor coefficients and emissivity factors were duplicated from the An et al. (2017) paper. This model output is returned in MJ/m^2, which must be converted to the proper units of W/m^2 to be used in the PM equation, the surface heat storage submodel, and the surface resistance submodel. Overall, this net radiation term addresses exchanges of solar energy, not accounting for the anthropogenic heat additions in urban areas. Therefore, the anthropogenic heat flux must also be calculated and incorporated as shown in the PM equation and subsequent subsections.

The saturation vapor pressure, e_d, can be calculated using:

$$e_d = 0.611\exp\left(\frac{17.27T}{T+237.3}\right) \quad (5)$$

To quantify R_{so} we use the formula:

$$R_{so} = (0.75 + 0.0002EL)(R_{sa}) \quad (6)$$

where EL is elevation of watershed centroid (m) obtained from Google Earth Pro, and R_{sa} is given by:

$$R_{sa} = \left[\frac{24(60)}{\pi}\right] G_{sc} d_r (cos\phi cos\delta sin\omega_s + \omega_s sin\phi sin\delta) \quad (7)$$

$$d_r = 1 + 0.033\cos\left(\frac{2\pi J}{365}\right) \quad (8)$$

$$\delta = 0.4101\cos\left[\frac{2\pi(J-172)}{365}\right] \quad (9)$$

$$\omega_s = \cos^{-1}(-tan\phi tan\delta) \quad (10)$$

where G_{sc} is the solar constant (0.08202 MJ/m^2/min), d_r is the relative distance between the Earth and the Sun (m), ϕ is the latitude (radians), δ is the solar declination (radians), ω_s is the solar time angle (radians), and J is the Julian day, or numbered day between 1 and 365 (366 for leap years) indicating the day of year.

2.3.3 Q_F, Anthropogenic Heat Flux

This term is a measure of the contribution of anthropogenic activities to total heat flux in urban areas. It is a quantity that represents the heat released by building air conditioning, vehicle transportation, and human metabolism. A study by Sailor et al. (2015) was performed to create a national database of anthropogenic heat flux. Regression models were also created to estimate the anthropogenic heat flux in any city based on two factors. The equations were created by quantifying anthropogenic heat flux in 61 cities across the continuous United States, and through

multiple linear regression, heating degree days and population density were revealed to be the dominant factors influencing this term. The authors provide the seasonal regression equations with seasonal coefficients to estimate a maximum anthropogenic heat flux based on the heating degree days in a single month, meaning the daily maximums calculated only apply to that specific month. A non-dimensional hourly profile is included that allows for hourly estimates that can be summed to calculate daily anthropogenic heat flux and is shown in Table 3. In this study, the database created by Sailor et al. (2015) will be used for final monthly estimates of anthropogenic heat flux. The regression equations are as follows:

$$Q_{Fmax}(summer) = \beta 0 + PopDens * \beta 1 \quad (11)$$

$$Q_{Fmax}(winter, spring, autumn) = \beta 0 + PopDens * \beta 1 + HDD * \beta 2 \quad (12)$$

where β0, β1, and β2 are coefficients for regression models found in Table 4, PopDens is the population density of area of interest in persons per square kilometer within the watershed, and HDD is monthly heating degree days. Because the study area has less than 4000 °C in a year of heating degree days, the South River watershed is considered to have a warm winter climate. The formula for HDD is found in Sailor and Vasireddy (2006):

$$HDD = \gamma_1(T_b - T) \qquad \gamma_1 = 1.0 \;\; if \; (T_b - T) \geq 0, \quad (13)$$

$$0.0 \;\; if \; (T_b - T) < 0$$

where T_b is the standard base temperature of 18.3 °C (65 °F) and T is air temperature. The unit for HDD is °C per unit time, where temperatures can be analyzed at hourly, daily, monthly, or annual time scales. Calculations here require units of °C/month, so daily HDD are calculated and aggregated for each month of the year because only daily temperature data were available. On a plot of temperature vs. time, the area between the base temperature line and the actual

temperature represents demand for air conditioning. The area below the base temperature line is referred to as the heating degree days (HDD) as it is indicative of demand for heating. Conversely, if the air temperatures are above the base temperature line, these are considered cooling degree days (CDD). With this fact known, as well as only requiring HDD in the regression equations, if the temperature is above the base temperature, the day's HDD is multiplied by a unitless term, y_1, of zero and not accounted for in the total monthly HDD. If the temperature is below the base temperature, HDD is multiplied by a y_1 of one to keep the HDD in the aggregated monthly total. Although there is a method presented to model the anthropogenic heat flux, the study uses the database of monthly values created by Sailor et al. (2015).

Table 3: Hourly non-dimensional heating profiles used in this study obtained from Sailor et al. (2015).

Hour	Summer profile	Winter profile	
		Cold winter cities	Warm winter cities
1	0.25 Qf_{max}	0.37 Qf_{max}	0.28 Qf_{max}
2	0.23 Qf_{max}	0.35 Qf_{max}	0.26 Qf_{max}
3	0.25 Qf_{max}	0.35 Qf_{max}	0.25 Qf_{max}
4	0.21 Qf_{max}	0.34 Qf_{max}	0.25 Qf_{max}
5	0.22 Qf_{max}	0.35 Qf_{max}	0.26 Qf_{max}
6	0.29 Qf_{max}	0.40 Qf_{max}	0.34 Qf_{max}
7	0.53 Qf_{max}	0.62 Qf_{max}	0.58 Qf_{max}
8	0.82 Qf_{max}	0.86 Qf_{max}	0.87 Qf_{max}
9	0.87 Qf_{max}	0.95 Qf_{max}	0.92 Qf_{max}
10	0.80 Qf_{max}	0.89 Qf_{max}	0.84 Qf_{max}
11	0.80 Qf_{max}	0.88 Qf_{max}	0.83 Qf_{max}
12	0.84 Qf_{max}	0.91 Qf_{max}	0.86 Qf_{max}
13	0.89 Qf_{max}	0.93 Qf_{max}	0.90 Qf_{max}
14	0.89 Qf_{max}	0.93 Qf_{max}	0.90 Qf_{max}
15	0.93 Qf_{max}	0.96 Qf_{max}	0.93 Qf_{max}
16	1.00 Qf_{max}	1.00 Qf_{max}	1.00 Qf_{max}
17	0.90 Qf_{max}	0.89 Qf_{max}	0.90 Qf_{max}
18	0.78 Qf_{max}	0.77 Qf_{max}	0.79 Qf_{max}
19	0.56 Qf_{max}	0.58 Qf_{max}	0.57 Qf_{max}
20	0.48 Qf_{max}	0.52 Qf_{max}	0.50 Qf_{max}
21	0.44 Qf_{max}	0.49 Qf_{max}	0.45 Qf_{max}
22	0.41 Qf_{max}	0.47 Qf_{max}	0.43 Qf_{max}
23	0.36 Qf_{max}	0.44 Qf_{max}	0.39 Qf_{max}
24	0.30 Qf_{max}	0.40 Qf_{max}	0.33 Qf_{max}

Table 4: Coefficients for seasonal anthropogenic heat flux regression models from Sailor et al. (2015) with corresponding root mean squared error (RMSE) and coefficient of determination (R2).

Season	β0	β1	β2	RMSE (W/m^2)	R^2
Winter	-6.638	0.010	0.009	3.94	0.94
Spring	-0.160	0.007	0.007	2.84	0.95
Summer	2.554	0.000	0.007	2.89	0.94
Autumn	0.618	0.006	0.007	2.70	0.95

2.3.4 ΔQ_s, Storage Heat Flux

This term describes how land surfaces retain radiant energy from day to day. As AET is largely dependent on the magnitude of solar radiation (Monteith, 1965), it is important to address antecedent energetic conditions. Storage heat flux is estimated using the objective hysteresis model formulated by Grimmond and Oke (1999) that incorporates the delayed nature of the storage heat flux and properties of specific land surfaces:

$$\Delta Q_s = a_1 R_n + a_2 \frac{\partial R_n}{\partial t} + a_3 \quad (14)$$

$$\frac{\partial R_n}{\partial t} = 0.5(R_{n_{t+1}} - R_{n_{t-1}}) \quad (15)$$

where a_1, a_2, and a_3 are constant terms indicated by experimental study and R_n is net radiation. The a_1 term indicated overall strength of dependance of the storage flux on net radiation. It is known to increase with impervious landcover and decrease with vegetative cover. The a_2 term indicates the degree and direction of the phase relations between R_n and ΔQ_s. The a_3 term is an intercept that indicated the relative timing when R_n and ΔQ_s turn negative. Terms a_1, a_2, and a_3 chosen for this study are as indicated by Grimmond and Oke (2002) based on landcover. The table for these values is included as Table 5.

Table 5: Coefficients used in OHM model found in Grimmond and Oke (2002).

Surface type	Sites where used	Basis for values	a_1	a_2 (h)	a_3 (W m^{-2})
(a) Coefficients used in current application					
Green space/open	All	Mean of all seven sources in Table 4 (Grimmond and Oke 1999c)	0.34	0.31	−31
Paved/impervious	All	Mean of all five sources in Table 4 (Grimmond and Oke 1999c)	0.70	0.33	−38
Rooftop	A93, A94 Sg94, S91u, Vs89, Vs92, T90	Mean of 9, 10, 11; see (b)	0.10	0.26	−4
	C95u	Mean of 9, 11; see (b)	0.11	0.30	−6
	Me93	Mean of 5, 8, 11, 12; see (b)	0.11	0.45	−8
	Mi95	Mean of 9, 10; see (b)	0.11	0.25	−4
	C92	Mean of 5, 8, 9, 11; see (b)	0.13	0.45	−9
	Vl92	Mean of 5, 8; see (b)	0.16	0.60	−12

(b) Roof type

	Code referred to in (a)	Source	a_1	a_2 (h)	a_3 (W m^{-2})
Vancouver (tar and gravel)	2	Yap (1973)	0.17	0.10	−17
Uppsala	3		Not recommended (Meyn 2000)		
Kyoto	4		Not recommended (Meyn 2000)		
Gravel, tar, concrete flat industrial (avg)	5	Meyn (2000)	0.25	0.92	−22
Gravel, tar, concrete flat industrial (dry)	6	Meyn (2000)	0.25	0.70	−22
Gravel, tar, concrete flat industrial (wet)	7	Meyn (2000)	0.25	0.70	−22
Bitumen spread over flat industrial membrane	8	Meyn (2000)	0.06	0.28	−3
Asphalt shingle–on-plywood residential roof	9	Meyn (2000)	0.14	0.33	−6
High-albedo asphalt shingle residential roof	10	Meyn (2000)	0.09	0.18	−1
Ceramic tile	11	Meyn (2000)	0.07	0.26	−6
Slate tile	12	Meyn (2000)	0.08	0.32	0

2.3.5 C_a, Specific Heat of Air

The specific heat of air represents the amount of energy required to increase the air temperature by one dree at a constant pressure and depends on the humidity of the air. The specific heat of air is often assumed to be 1.00 x 10^{-3} MJ/kgK (Dingman, 2002). A more specific value of 1006 J/m^3/^{o}C is also appropriate and is used in this study.

2.3.6 V, Vapor Pressure Deficit

The vapor pressure deficit is the difference between the saturation vapor pressure and the vapor pressure of air, which can be an important driver of atmospheric water demand for plants, thus effecting AET rates. How AET responds to the vapor pressure deficit depends on climate, photosynthesis strategy, and plant type (Massmann et al., 2019). The formula for vapor pressure deficit is as follows:

$$V = e^* - e \quad (16)$$

$$e^* = 0.611\exp\left(\frac{17.27T}{T+237.3}\right) \quad (17)$$

$$e = \frac{RH}{100} * e^* \quad (18)$$

where RH is relative humidity as a percentage and T is temperature (°C) obtained from the GAEMN.

2.3.7 R_a, Aerodynamic Resistance

The aerodynamic resistance term quantifies transfer of heat and water vapor from the evaporating surface into the air above canopy. This term is a function of wind speed, atmospheric stability, and surface roughness; and the higher the aerodynamic resistance of a given feature, the lower final AET estimates will be (Penman & Schofield, 1951). The aerodynamic resistance of a surface is inversely proportional to atmospheric wind speed and shows considerable diurnal variation (S. Liu et al., 2006). The daily values obtained here will be a possible source of error in AET estimates because the diurnal patterns were not addressed. Grimmond and Oke (1999) state that the urbanized PM equation is not sensitive to the method of calculating r_a, therefore, we estimate the term by using the equation found in Shuttleworth (2007):

$$r_a = \frac{\ln\left[\frac{z_m-d}{z_{om}}\right]\ln\left[\frac{z_m-d}{z_{om/10}}\right]}{k^2 u_z} \quad (19)$$

where z_m is the height of wind and humidity measurements [m], d is the zero plane displacement height [m], z_{om} is the roughness length governing momentum transfer [m], k is von Karman's constant, 0.41, and u_z is the wind speed at height z [m/s]. This equation is limited to neutral conditions, which is a limitation of this equation. Because the heights of the roughness features

are much taller in urban areas, wind speed originally taken at roughly 3 meters above the ground must be extrapolated to roughly 30 meters above the ground using the vertical wind profile power law in Spera and Richards (1979):

$$u = u_r \left(\frac{z}{z_r}\right)^{\alpha} \quad (20)$$

where u is the extrapolated wind speed, u_r is the original wind speed, z is the height at which the new windspeed is calculated for, z_r is the height of original wind measurement, and α is coefficient that varies depending on stability of the atmosphere. The α coefficient is assumed to be 0.143 over land surfaces and 0.11 over open water in neutral conditions, which is used in this study.

Using the Rule of Thumb method described by Grimmond and Oke (1999), the variables d and z_{om} can be estimated using the following equations:

$$d = 0.5 z_H \quad (21)$$

$$z_{om} = 0.1 z_H \quad (22)$$

where z_H is the average height of features in the landcover class.

2.3.8 r_s, Surface Resistance

The surface resistance describes the resistance of vapor flow exiting through stomata on a leaf body, or more generally the resistance to facilitate water vapor transfer into the air from any surface. Environmental factors affecting surface resistance includes solar radiation, absolute-humidity deficit, air temperature, soil-moisture deficit, and leaf area index of vegetation, and as surface resistance increases, total AET decreases due stresses on the plant leaf in any number of the controlling environmental factors (Boegh et al., 2002; Jarvi, 1976; S. Irmak & D. Mutiibwa,

2009; Stewart, 1988). Sumner and Jacobs (2005) conducted a multiple linear regression analysis to determine which environmental variables impacted surface resistance the most and found that net radiation and vapor pressure deficits are most responsible for variability. The procedure is as follows:

$$g_{max} = 5.39x10^{-5}R_n + 0.0033 \quad (23)$$

$$f(D) = -0.166\ln(D) + 0.235 \quad (24)$$

$$g_s = \frac{g_{max}}{f(D)} \quad (25)$$

$$r_s = \frac{1}{g_s} \quad (26)$$

where g_{max} is the maximum surface conductance (m/s), R_n is net radiation (W/m^2), D is the vapor pressure deficit (kPa), g_s is the surface conductance (m/s), and r_s is the surface resistance (s/m).

The surface resistance is considerably dependent of the wetness of the surface. It has been shown that the surface resistance of a wet surface is always zero (Shuttleworth, 1978). A proposed surface resistance model to address the transitions between wet, partially wet, and dry surfaces is available in Shuttleworth (1978) and used by Grimmond and Oke (1991), but some data parameters required, in addition to data to model those parameters, were not available. An example of data not available includes frictional velocity. Therefore, we use the regression models presented in equations 23-26 to model surface resistance, regardless of surface wetness. Mathematically, setting surface resistance to zero increases PM AET estimates because the denominator is decreased. The possible underestimation of AET resulting from the surface resistance submodel is thought to be offset by canopy storage accounting as detailed in section 2.4.

2.3.9 γ, Psychometric Constant

The psychometric constant is a term that relates the partial pressure of water in the air to the air temperature. Since atmospheric pressure, P, depends on altitude, so does the psychometric constant. At higher altitudes water can evaporate and boil at lower temperatures, so this term is important to include in the Penman-Monteith equation. Contrary to the name, the psychometric constant is not actually a constant. It most readily varies with temperature and is given by the expression found in Dingman (2002):

$$\gamma = \frac{c_a P}{0.622\lambda_v} \quad (27)$$

where c_a is the specific heat of air, 1.00 x10^{-3} MJ/kg/K , P is atmospheric pressure in kPa obtained from GAEMN, and λ_v is latent heat of vaporization MJ/kg. Latent heat of vaporization is estimated by the following equation:

$$\lambda_v = 2.50 - 2.36x10^{-3} * T \quad (28)$$

where T is temperature in ^{o}C obtained for the GAEMN. The resulting units of the psychometric constant are in kPa/K. Converting this quantity to Pa/K are required for use in this proposed Penman-Monteith approach.

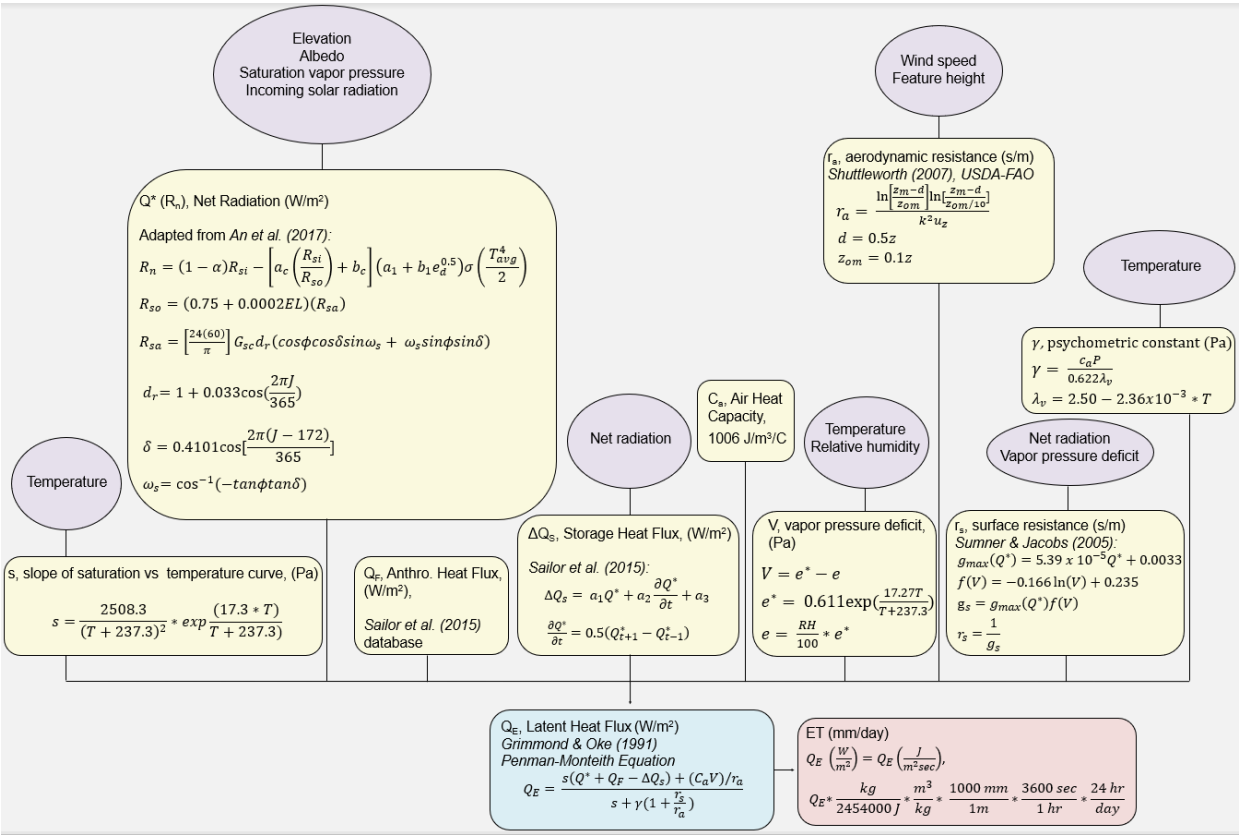

Figure 4: PM procedure for daily AET estimation. Diagram includes data required for each submodel (purple ovals), component processes (yellow rectangles), Penman-Monteith equation (blue rectangle), and procedure to convert from latent heat flux to a depth of AET per day using the latent heat of vaporization of water (2,454,000 Joules/kilogram) (red rectangle).

Table 6: All data required for the daily AET estimation presented in this study using the PM procedure and regression models. Daily averages of meteorological data from respective stations were used.

Symbol	Description	Units
ϕ	Latitude	radians
EL	Elevation	meters
T_n	Minimum temperature	°C
T_m	Maximum temperature	°C
T	Average temperature	°C
R_{si}	Incoming solar radiation	MJ/m²/day
α	Albedo of LC surface	-
RH	Relative humidity	%
u_{zi}	Wind speed at height i	meters/sec
z	Height of features in LC class	meters

2.4 Accounting for Land Cover Surface Water Availability

As mentioned in earlier sections, the PM method alone does not address the water availability of each land surface type. This fact can lead to overestimations of AET because the

AET calculated by the PM equation is not constrained by any possibly water-limiting conditions. To accurately represent AET in an urbanized watershed, the surface moisture conditions must be considered. A general water balance equation is shown in Equation 29 from Grimmond and Oke (1991) to assess the current state of water storage in each land cover.

$$\frac{dC}{dt} = (P + I) - (D - AET) \quad (29)$$

where P is precipitation, I is piped water supply (i.e. irrigation), D is drainage, and AET is evapotranspiration. A procedure similar to that found in Grimmond and Oke (1991) and Järvi et al. (2011) is used to quantify drainage of each land surface type with respect to surface-specific parameters, incoming hourly precipitation, seasonal irrigation, and antecedent water storage conditions. When the term (D + I) is larger than (P + I), surface storage becomes negative. Since negative storage is not possible, negative storage estimates are taken as 0. In vegetated land cover classes, it can be assumed that even if the surface storage is 0 mm, the PM AET comes from deep water storage and accessed by root systems, leaving vegetated PM AET estimates unchanged. This assumption means that the surface water availability model is not applicable in vegetated land covers, only impervious cover. In impervious land cover classes, the surface water accountability becomes much more important because water that does not infiltrate into the ground surface becomes runoff, moving water to other areas. This water transfer removes water from impervious land cover classes that would have evaporated and is no longer there. Therefore, if the calculated surface storage for impervious classes is lower than the PM AET estimate, PM AET estimates are adjusted down to the storage availability to reflect the water-limiting conditions of impervious land cover. The equation to calculate drainage on unirrigated, vegetated areas is as follows:

$$D = D_o \exp\left[(bC) - 1\right] \quad (30)$$

where D_o is the drainage rate when the water capacity equals storage, b is an empirical coefficient, and C is the storage capacity of that hour, calculated by subtracting the previous time-step's drainage from the current precipitation amount. Forest and short vegetation/shrub land were grouped together for the water surface availability procedure to create one canopy storage equation because there were not specific parameters for shrubland, in addition to being vegetated but not irrigated. In impervious and irrigated (grassland) land cover types, an alternative equation is used to quantify the drainage:

$$D = D_o(C_{t-1})^b \quad (31)$$

The water storage equations are executed at an hourly time-step. This detail is crucial because the empirical coefficients and initial drainage estimates are calibrated at an hourly time step in the referenced papers (Grimmond & Oke, 1991; Järvi et al., 2011). Hourly precipitation was obtained from a station within the SRW at Hartsfield-Jackson International Airport. Where it is required, daily AET estimates produced by the PM AET method are scaled by incoming hourly solar radiation. A proportion of hourly incoming solar radiation to total daily radiation was used to create a continuous proportional hourly profile for every day. The daily PM AET estimates of each land cover type were distributed by multiplying each day PM estimate by hourly proportions of solar radiation, allowing for the creation of a continuous hourly AET estimates within each land cover. As shown in Grimmond and Oke (1991), Table 7 shows the land cover specific parameters required for the canopy storage models. An average of the building and pavement values and forest type values were used for developed land covers and forest/shrubland land covers, respectively. It is also assumed that all grass cover in the SRW is irrigated since detailed spatial and temporal irrigation information was not available.

Table 7: Surface water availability parameters specified by land cover as depicted in Grimmond and Oke (1991).

	Surface Characteristics					
	Pavement	Building	Coniferous	Deciduous	Unirrigated Grass	Irrigated Grass
S, mm	0.48	0.25	1.2	0.3	1.3	1.3
D function	7	7	5	5	5	7
Coefficient						
D_0	10	10	0.013	0.013	0.013	10
b	3	3	1.71	1.71	1.71	3
$C(t = 0)$	0.0	0.0	0.0	0.0	0.0	0.0

Municipal water usage was obtained through open records requests from the Scott Candler Water Treatment Facility. Data was acquired as daily estimates of water pumped for municipal use, and a ‘baseline’ use was calculated by taking the average of daily uses during the winter months for every year (December 1 through March 31). This ‘baseline’ quantity is thought to be the amount of water used within households regardless of the season throughout the year. At a daily time step, the averaged, baseline water use was subtracted from each day’s quantity of water pumped. The number returned from the subtraction is thought to be the amount of outdoor water use or irrigation for our purposes. If the result was a negative number, the day’s value was set to zero. The volume of water (m^3/day) calculated for each day was converted into a depth of irrigation water (mm/day) by dividing the outdoor water use by the area of grassland and converting the units to mm/day. Hourly estimates were created from dividing the daily values by 24 hr/day. It is assumed that the irrigation hourly rate is consistent throughout the day because the individual irrigation habits of households are not predictable. Lastly, the irrigation amounts from December 1 through March 31 in each year were set to zero as it is assumed no irrigation occurs in the winter months.

2.5 Regression AET Estimates

Regression models to estimate AET at a variety of time scales were obtained from published literature (Y. Fang et al., 2016a; Lu et al., 2003; Sanford & Selnick, 2013). The regression models presented are compared with TerraClimate reference AET estimates and PM AET estimates (Abatzoglou et al., 2018). The goal of a model comparison is to investigate if the chosen models could be used confidently to estimate AET in urban watersheds with heterogeneous landcover in a humid, subtropical climate.

2.5.1 Monthly AET Estimates

One monthly AET model employed in this study was created by Fang et al. (2015). Using eddy covariance AET and other meteorological parameters, the authors formulated three different regression models to estimate AET. These models best exhibit conditions in a monthly temporal resolution and separate land cover classes for calculations instead of lumping them. Type I models require potential evapotranspiration (PET), precipitation, net radiation, and leaf area index (LAI) data, whereas, Type II models only require PET, precipitation, and LAI data. LAI data, which were 8-day composites at 500-m resolution, were extracted from the MODIS MCD15A2H Leaf Area Index product (Myneni et al., 2015) for large, consistent areas of deciduous forest, evergreen forest, shrubland, and combined low-lying vegetation/grass areas in the Atlanta region. Type III models require precipitation, LAI, and the Food and Agriculture Organization (FAO) grass reference evapotranspiration (ETo). PET can be calculated through the Hamon equation detailed in Lu et al. (2005):

$$PET = k * 0.165 * 216.7 * N * (\frac{e_s}{T+273.3}) \quad (32)$$

where k is a unitless proportionality coefficient of 11, N is daytime length (x/12 hours), e_s is saturation vapor pressure calculated previously, and T is average monthly temperature in ^{o}C.

Long-term records of daytime length in minutes were acquired from the NOAA's National Centers for Environmental Information Global Surface Summary of the Day (GSOD) database.

The creators of the Fang methods determined that Type I and Type II were the best fitting models to reference evapotranspiration measurements but suggest that Type II models be employed when net radiation data are not available. Land cover totals can be aggregated and weighted at the end of calculations with proportions of land-cover type to get an AET estimate of the complete study area. Tables of the Type I and Type II models separated by land cover type are depicted in Table 7 and Table 8, respectively. Regardless of type, the Fang et al. (2015) models do not have impervious land cover equations. To remedy this, a percentage of precipitation is used as 'impervious AET.' Based on published literature, impervious surfaces contribute varying percentages of precipitation lost to evaporation; it's as low as 16% in one location and as much as 29% in another in Zhou et al. (2021). The other papers report 21-24% (Ragab et al., 2003), 19% (Davies, 1981), and 17% (Cohard et al., 2018). A median value of 19% was used, meaning 19% of the precipitation observed each month was added to the Fang model estimates to more accurately depict AET in an urbanized watershed.

Table 8: Type I models created by Fang et al. (2015) where ET is evapotranspiration (mm), PET is potential evapotranspiration (mm), LAI is leaf area index, Rn is net radiation (MJ/m^2) , RMSE is root mean squared error of the model performance, and R^2 is the model residual squared.

Landcover Type	Model by land cover	RMSE	R^2
Shrubland	ET= 0.51 + 0.03 * PET + 14.73 * LAI + 0.8 * Rn	14.0	0.79
Cropland	ET= 0.87 + 0.19 * Rn + 13.99 * LAI + 0.06 * P	23.9	0.73
Grassland	ET= 5.55 + 7.23 * LAI + 0.20 * Rn	16.3	0.79
Deciduous Forest	ET= -14.22 + 0.74 * PET + 0.10 * Rn	22.2	0.77
Evergreen needle leaf forest	ET= 3.00 + 0.30 * PET + 3.99 * LAI + 0.09 * Rn	17.1	0.71
Evergreen broad leaf forest	ET= -0.15 + 0.47 * PET + 0.13 * Rn	13.3	0.86
Mixed forest	ET= -8.76 + 0.95 * PET	14.8	0.80
Savannas	ET= -8.07 + 33.46 * LAI +0.07 * Rn	14.0	0.66

Table 9: Type II models created by Fang et al. (2015) where ET is evapotranspiration (mm), PET is potential evapotranspiration (mm), LAI is leaf area index, P is precipitation (mm) , RMSE is root mean squared error of the model performance, and R^2 is the model residual squared.

Landcover Type	Model by land cover	RMSE	R^2
Shrubland	ET= -3.11 + 0.39 * PET + 0.09 * P + 11.127 * LAI	12.5	0.80
Cropland	ET= -8.15 + 0.86 * PET + 0.01 * P + 9.54 * LAI	20.9	0.70
Grassland	ET= -1.36 + 0.70 * PET + 0.04 * P + 6.56 * LAI	16.8	0.66
Deciduous Forest	ET= -14.82 + 0.98 * PET + 2.72 * LAI	23.7	0.74
Evergreen needle leaf forest	ET= 0.10 + 0.64 * PET + 0.04 * P + 3.53 * LAI	17.8	0.68
Evergreen broad leaf forest	ET= 7.71 + 0.74 * PET + 1.85 * LAI	16.8	0.76
Mixed forest	ET= -8.763 + 0.95 * PET	13.1	0.79
Savannas	ET= -25.66 + 0.18 * PET + 0.10 * P + 44.63 * LAI	11.1	0.68

2.5.2 Annual AET Estimates

The first annual model employed in this study is adopted from Lu et al. (2003) and analyzed against watershed water balance AET estimates. This evapotranspiration model is the simplest of all the models included in this study. Out of 23 environmental variables, extraterrestrial solar radiation, rainfall amount, latitude, elevation, forest cover, and presence of water bodies were deemed significant and included in a regression model to estimate annual AET. Water bodies were later removed because of their ability to decrease actual AET with increasing number of bodies. The remaining 22 variables were analyzed again to find that net radiation, rainfall, elevation, and forest are the most influential variables. Given limitations in acquiring extraterrestrial solar radiation, the authors postulated that latitude, rainfall, elevation, and forest cover were equally as influential on final estimates. Even though this equation is created from heavily forested watersheds, the authors show that the model performs well with sufficient confidence. In the end, accounting for only forested evapotranspiration may prove to be a source of error in final analysis. There is only one equation, and it assumes AET comes predominantly from forests in a watershed:

$$ET = 1098.786 + 0.0309\ Rainfall - 0.289\ Elevation - 21.840\ Latitude + 196\ Forest \quad (33)$$

where ET is annual actual evapotranspiration (mm), rainfall is mean annual precipitation (mm), latitude is the watershed latitude at the outlet (degree), elevation is mean watershed elevation (m), and forest is percentage coverage of forest cover of the watershed.

The model created by Sanford and Selnick (2013) is a regression equation created from watershed scale water balance AET data obtained from at least one catchment in each state across the continuous United States. Because this model was a long-term study, it was assumed

that change in annual water storage was negligible. The authors attempt to create a regression using just climate data but deemed that even though climate accounted for a lot of the AET variation observed, land cover was very important as well. The final regression equation incorporates climate and landcover data with good confidence (R^2= 0.882). The data used to create the regression equations were from 1971-2000, so this may prove to be a source of error in our final analysis. For now, we are assuming the equations will function similarly to their performance in the original application time frame. The equation returns a ratio of evapotranspiration to precipitation, but evapotranspiration can easily be derived by multiplying by precipitation. Table 10 shows the regression equation and other variables and constants one will require to complete the computations.

Table 10: Regression equation and supplemental equations for estimating annual evapotranspiration obtained from Sanford and Selnick (2013).

Regression equation	$ET/P = \Lambda(\tau\Delta/(\tau\Delta + \Pi))$ $\tau = (T_m + T_o)^m/((T_m + T_o)^m + a), \Delta = (T_x - T_n)/((T_x - T_n) + b), \Pi = (P/P_o)^n$
Climate variables	T_m, mean annual daily temperature (°C); T_x, mean annual maximum daily temperature (°C); T_n, mean annual minimum daily temperature (°C); P, mean annual precipitation (cm)
Land-cover variables	$\Lambda = (1 + cL_d + eL_f + hL_s + jL_g + kL_a + rL_m)$, where L_i is the fraction of landcover type i within the area of calculation, and subscripts d, developed; f, forest; s, shrubland; g, grassland; a, agriculture; m, marsh

	Climate Parameters						Land-Cover Parameters					
Parameter	*To*	*Po*	*m*	*n*	*a*	*b*	*c*	*e*	*h*	*j*	*k*	*r*
Parameter value for climate-only regression	13.735	505.87	2.4721	1.9044	10,000	18.262	0.000	0.000	0.000	0.000	0.000	0.000
Parameter value for climate- and land-cover-based regression	17.737	938.89	1.9897	2.4721	10,000	18.457	0.173	0.297	0.094	0.236	0.382	0.400

2.6 Rural Watershed AET

Estimates of AET from all the modelled procedures were compared with the water-budget AET at the reference watersheds, using the reference watershed AET to see which procedure was most accurate at those watersheds and to adjust the PM-derived estimates. In natural, undisturbed watersheds, evapotranspiration is commonly estimated as the difference between precipitation and streamflow, neglecting long-term changes in storage (Vörösmarty et al., 1998). For simplicity, we assume that there is no net movement of groundwater into or out of the

watersheds. The water balance method has been proven to be useful at a watershed scale (Sloto & Buxton, 2005). In undeveloped watersheds, infrastructure-mediated flows common to urban environments, like irrigation, pipe leakage, reservoir withdrawal, and inflows into sewer systems, are not present. Precipitation data are monthly estimates obtained from the PRISM database and discharge data are from the United States Geological Survey (USGS). A recent study compared PRISM to high-quality gauges and found that in the Southeast PRISM might overestimate precipitation by 3.25% (Buban et al., 2020). PRISM precipitation totals were adjusted by dividing by 1.0325. Reference watershed PM AET estimates were compared to water-balance AET to analyze how urbanization has affects watershed in the Piedmont region.

Additionally, each AET model's estimates were aggregated appropriately and compared on an annual timescale with remotely sensed TerraClimate data. TerraClimate data has a 4-km resolution, and estimates were acquired by placing 1,000 points randomly within the SRW and using the mean value of those points. This reference dataset uses interpolation that combines high-spatial resolution climatological normals from the WorldClim dataset with coarser spatial resolution, but time-varying data from CRU Ts4.0 and the Japanese 55-year Reanalysis (JRA55) (Abatzoglou et al., 2018). The result is a high-spatial resolution dataset that covers a broad temporal record.

3 RESULTS

3.1 Synopsis of Meteorological Trends

The SRW has experienced interesting meteorological trends, but firstly, there is no notable trend in long-term annual precipitation totals (Figure 5). While there are some notable years of high or low precipitation shown in Figure 5, where across years the annual-total precipitation varies by a factor of more than two (2007 versus 2009). Precipitation relative differences of 50-60% among years are also common. There was a strong, positive trend of average annual temperature, which was statistically significant ($\tau b = .305$, $p = .0299$) (Figure 5). Average daily incoming solar radiation by year is depicted in Figure 6. The graph shows a notable decreasing trend in daily incoming solar rates, which tested to be statically significant ($\tau b = -0.411$, $p = 0.006$). Lastly, Figure 7 shows that vapor pressure deficit stays consistent throughout the study period of 2001-2020 ($\tau b = -0.084$, $p = 0.302$). For the reference watersheds described in section 2.6, adjusting precipitation impacts the water budget AET, but in general changing precipitation does not have a large impact on the PM estimates as it is only an input in the surface water availability submodel (Section 2.4). Variation in precipitation amount strongly modulates evaporation from impervious surfaces as simulated in the PM model due to their marginal water-storage capacity. As mentioned previously, the vegetation is assumed to evaporate the full PM AET estimate due to root-soil water and groundwater access, thus the surface water availability model is only applicable to the impervious land cover. These surfaces that are mostly absent from the reference watersheds.

The reference watersheds did not observe the same incoming solar radiation trends. Neither Falling Creek watershed or Fausett Creek watershed observed any long-term change in incoming solar radiation using an α value of 0.01 or 0.05.

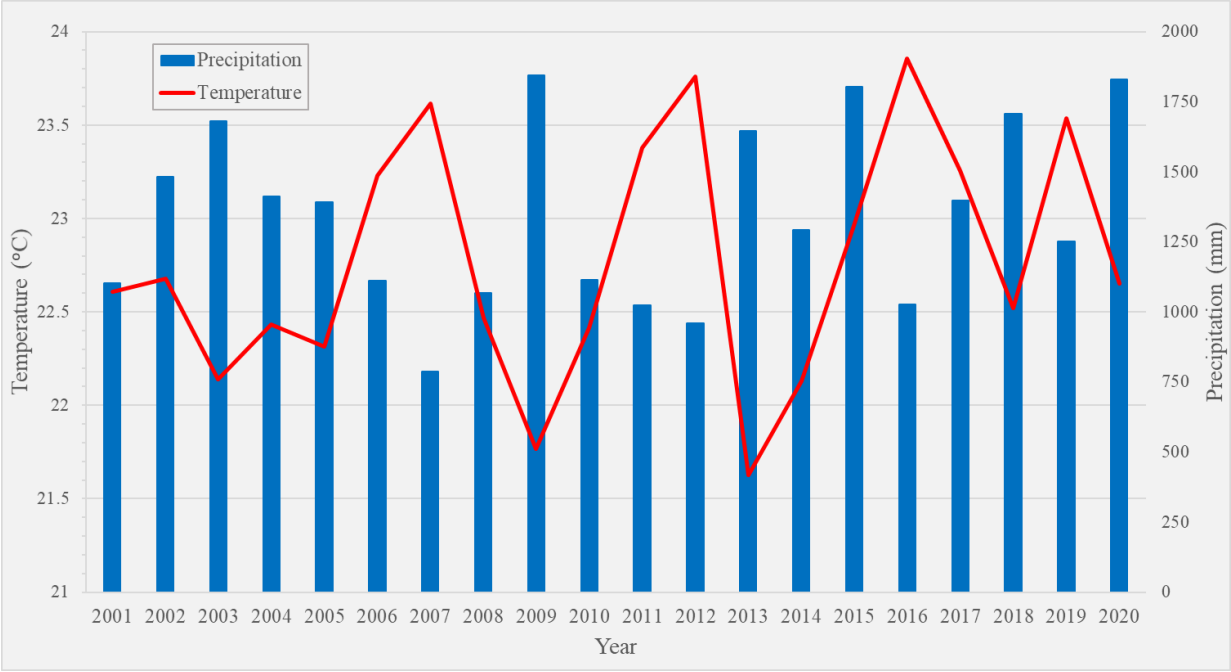

Figure 5: Long-term annual average daily temperature and annual precipitation totals of the SRW from 2001-2020. Temperature data from GAEMN, and precipitation is data collected at the ATL Hartsfield-Jackson Airport.

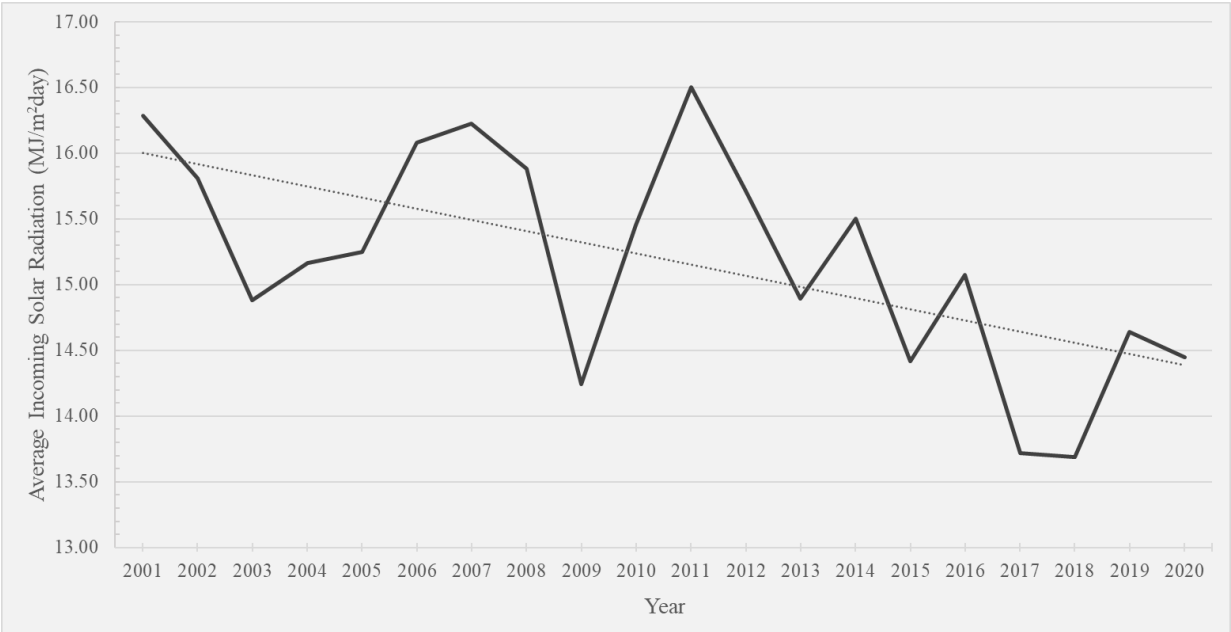

Figure 6: Long-term annual average of SRW daily rates of incoming solar radiation from GAEMN weather stations (p = 0.006).

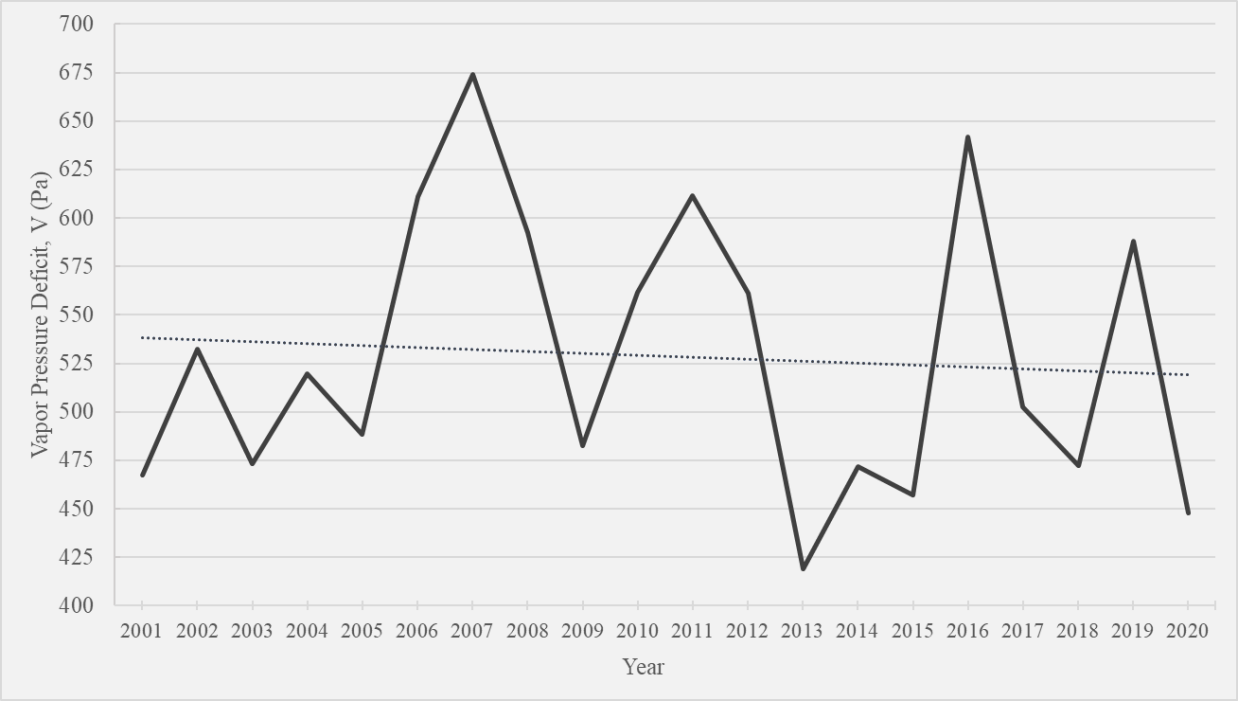

Figure 7: Long-term annual average of SRW vapor pressure deficit calculated by temperature dependent equations described in section 2.1.6 (p= 0.302).

3.2 Land Cover Analysis

There was considerable heterogeneity within the NLCD land cover classes (Figure 8). The composition of each land cover class and the resulting areas of each land cover type from 2001-2020 can be found in Appendices B and C, while 95% confidence intervals of area composition of the developed classes (21-24) can be found in Appendix E. The analysis revealed that NLCD developed classes 21-24 had 48.2%, 24.3%, 13.8%, and 4.4% forest cover, respectively. Developed classes 21-24 also had 28.5%, 42.9%, 21.5%, and 7.0% grass cover, respectively. Finally, it was found that the developed classes 21-24 contained 17.8%, 33.7%, 64.4%, and 84.8% impervious cover, respectively. These results show that the NLCD developed land cover classes contain a considerable amount of heterogeneity, consistent with the land cover composition definitions from the NLCD. From class 21 to 24, a stark increase in impervious cover is observed, where the amount of forest cover decrease but less drastically. An increase in

grass cover was observed in class 22, low-intensity developed, but there was a general decrease in grass cover as development intensity increases.

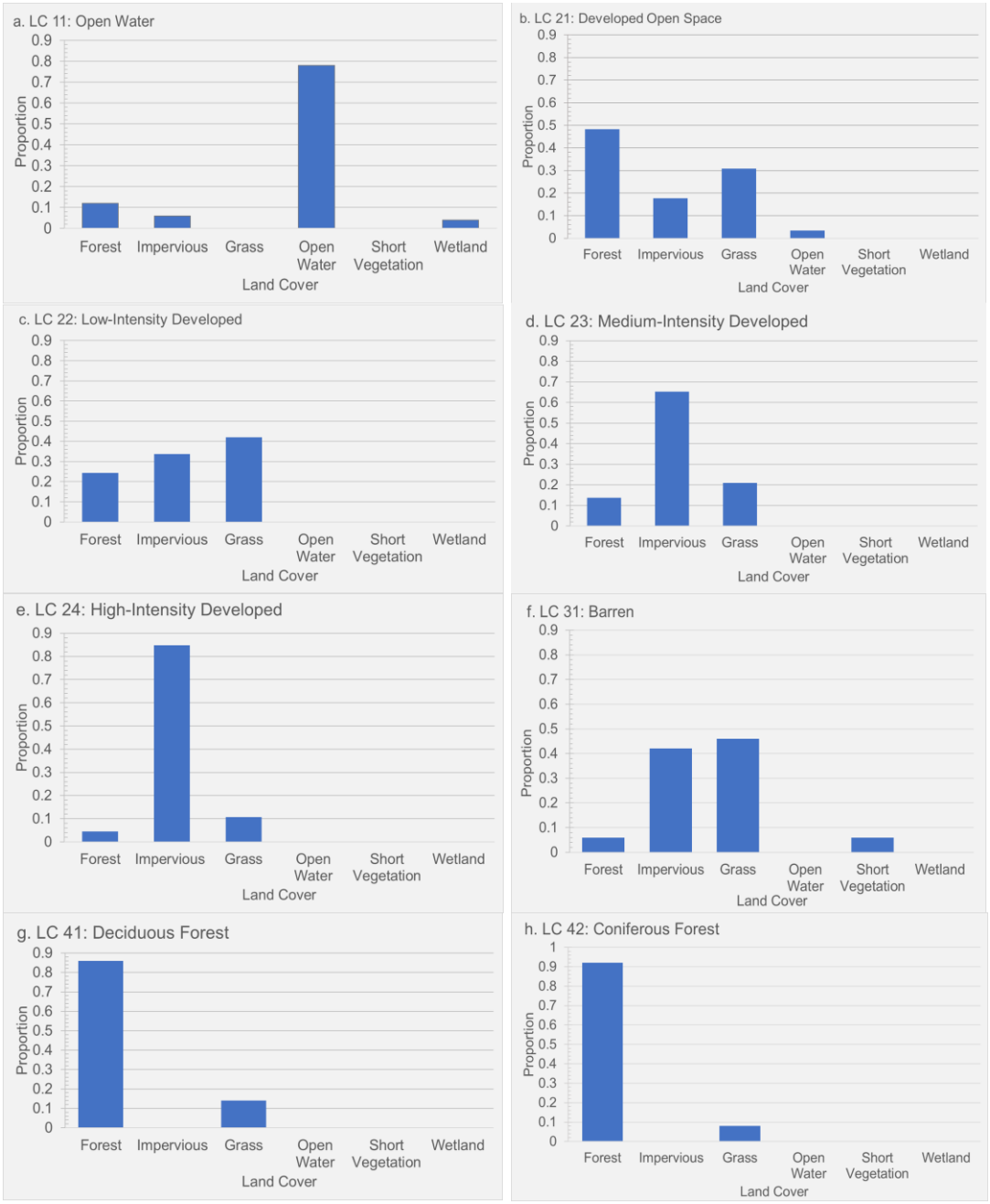

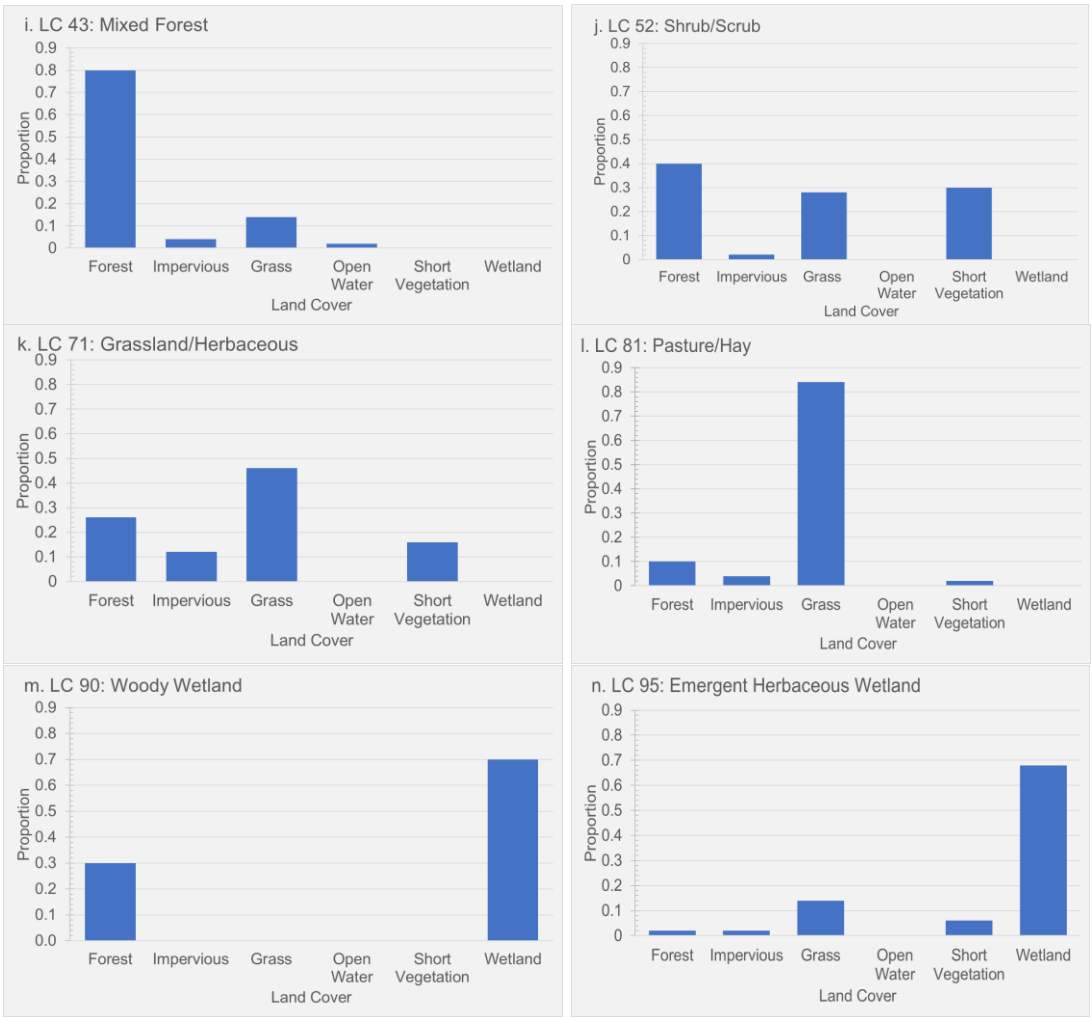

Figure 8: NLCD 2019 original classes' actual land cover (LC) distribution after manual land cover analysis (a-n). Proportion is calculated as the proportion of points of observed LC to total number of points in sample size. Proportions of each LC type in each class is multiplied by original area to calculate estimates of actual LC area within the South River watershed (SRW). All areas of the same LC types are aggregated to describe 6 total LC types within the entire SRW.

3.3 Penman-Monteith Approach

Within the SRW and including all land cover types, the PM approach returned a daily minimum value of 0.319 mm/day in the winter months and a daily maximum value of 5.12-5.24 mm/day in the summer months (Figure 9; Figure 10). The results are displayed before and after accounting for surface water availability, showing the intra-annual variability throughout the study period. It is shown that even before accounting for surface water availability (Figure 9) and

after (Figure 10), SRW AET in summer was roughly three times larger than in winter. Overall, the surface water availability procedure had a moderate effect on the PM AET estimates, decreasing the SRW long-term annual average AET from 866.45 mm/yr to 798.91 (+/- 37.66 mm/yr, Table 12), approximately a 7.8% reduction. Figure 10 shows a slight suppression in maximum AET values when compared to Figure 9, but the minimums remain unchanged. For vegetated surfaces, the surface water availability procedure had no effect. It is observed that as AET estimates increase, the range of possible estimate also increase (Figure 11), helping to illustrate the impact of that water-balance calculation on the AET estimates on days where estimates are high, namely the summertime.

The PM AET reductions came from using the surface water availability procedure on the developed cover, where it is known that if the surface has no surface water in storage, there is absolutely no water there to evaporate. Too many assumptions for vegetated covers would have to be made otherwise, like soil moisture, vegetation rooting depth, and more. Because the vegetated AETs are not adjusted when the surface water availability is lower than the PM AET estimates, it is assumed that the AET observed for every hour is a result of transpiration, and not evaporation from leafed surfaces. Surface water availability procedures were not done on the water and wetland land cover types, and therefore the PM AET estimates for those land cover classes are used unadjusted, as it is assumed they have water-unlimited conditions.

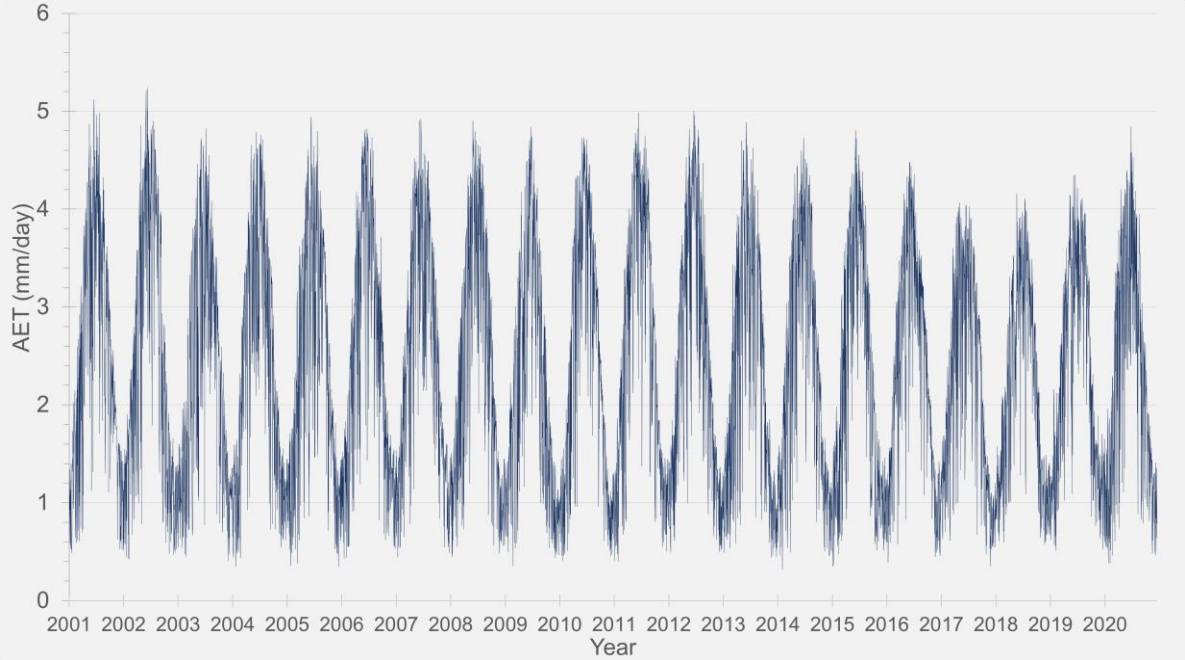

Figure 9: South River watershed daily AET estimates using the PM method from January 1, 2001 to December 31, 2020 before the surface water availability procedure.

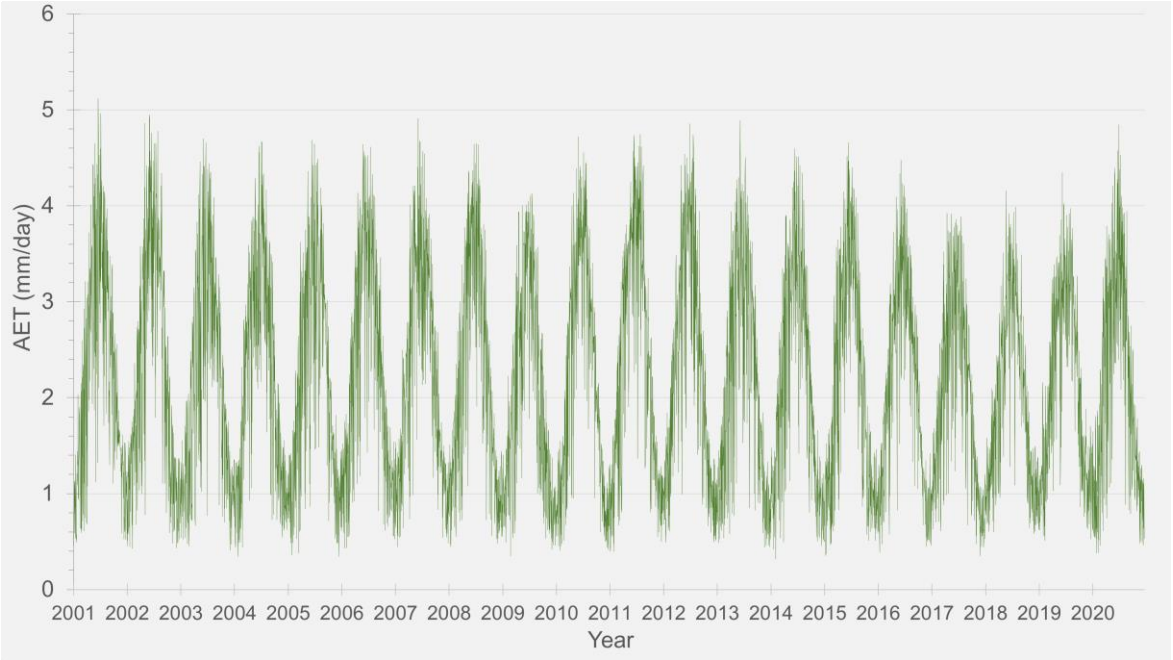

Figure 10: South River watershed daily AET estimates using the PM method from January 1, 2001 to December 31, 2020 after the surface water availability procedure.

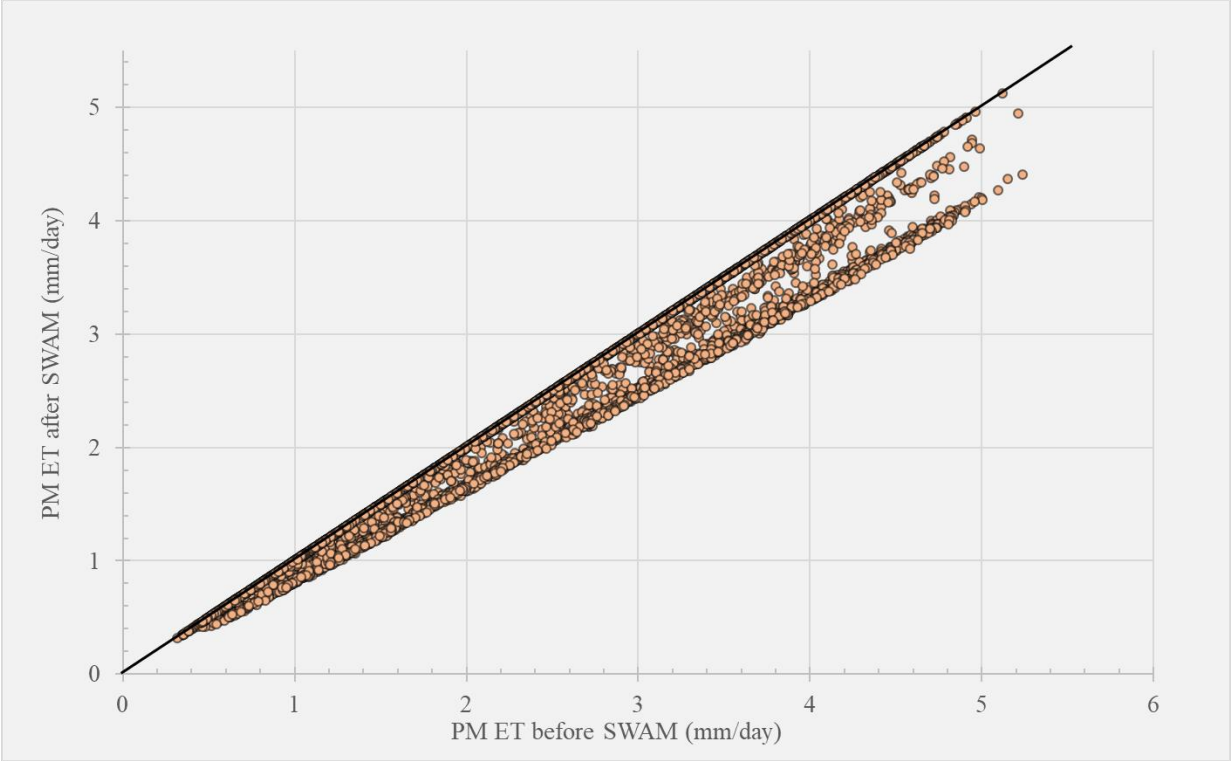

Figure 11: Scatter plot of PM daily AET before the surface water availability model (SWAM) and after SWAM from January 1, 2001- December 31, 2020. A 1:1 line is depicted in black.

The PM AET within the SRW peaks in the month of July with a long-term average of 105.88 mm (Figure 12). Estimates of monthly PM AET are the lowest in the month of December with a long-term average of 28.99 mm. In general, the incorporation of the canopy storage balance model decreased the interquartile range of possible monthly values, meaning less variation can be expected over time. Throughout the year, the skewness of the resulting estimates changes. In the colder months, PM AET is typically negatively skewed, meaning that more estimates are above the mean value than below. Alternatively, the data is slightly positively skewed in warmer months, meaning that more estimates are below the mean than above.

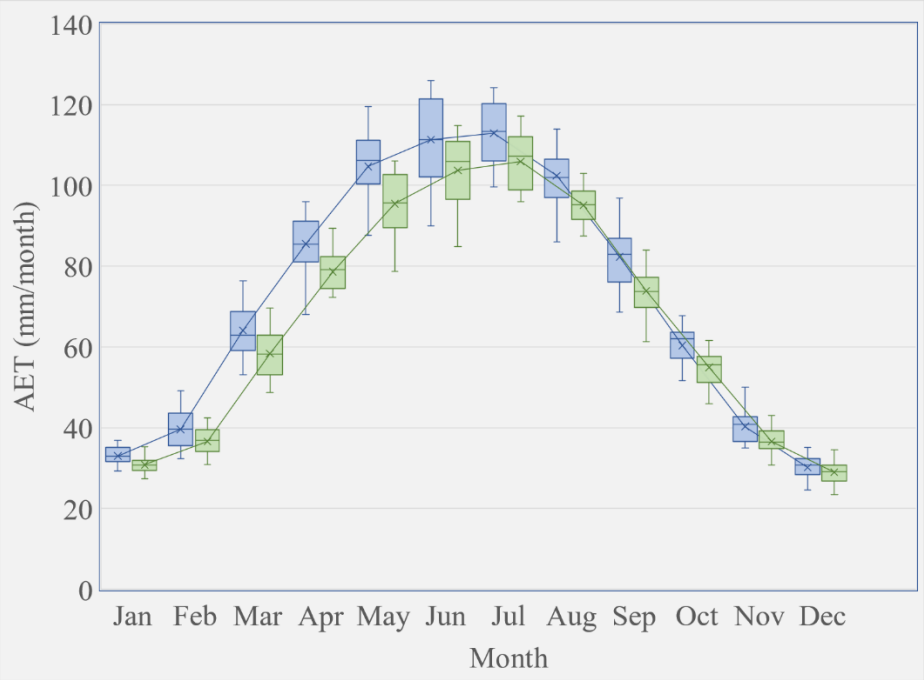

Figure 12: South River watershed average monthly AET estimates of PM without surface water availability, blue; PM with surface water availability, green from January 1, 2001, to December 31, 2020.

Additionally, Figure 13 depicts the composition of both total land cover within the SRW and contributions of each land cover type to total SRW AET. Our results suggest that while developed impervious areas account for 26.5% of the total land cover after manual land cover analysis, this land cover type only contributes 9.8% of the total SRW AET annually. The original percentage, before the surface water availability model, of developed AET was much larger at 16.8%. Additionally, it can be observed that grass land cover accounts for 26.5% of total area of the SRW, while it contributes a higher percentage to total AET, 33.2%. Forest cover accounts for 44.2% of total land cover in the SRW, and forests contribute over half the total AET for the study area at 52.4%. The remaining land cover types (short vegetation, open water, and wetland) display similar land area coverage and contributions to total AET.

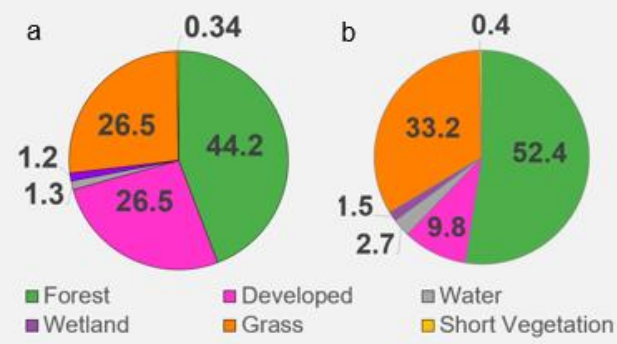

Figure 13: (a) Average percent coverage of land cover types within the SRW from 2001-2020, (b) Average percentage of AET that each land cover type contributes to total AET, within the SRW from 2001-2020 after the canopy storage water balance procedure.

Throughout the study period of 2001-2020, there is considerable variability in the SRW annual PM AET estimates (Figure 14); however the coefficient of variation only 4.7%. A lower coefficient of variation indicates that there is a lower amount of dispersion between all annual PM AET estimates. Figure 14 also shows the annual AET values and a trendline to visualize a strong, decreasing trend of annual AET throughout the study period within the SRW ($\tau b = -0.463$, $p = 0.002$). The maximum and minimum AET observed occurred in 2011 of 864.48 mm/yr and 2018 of 729.50 mm/yr, respectively, where this range is 10% of the annual average precipitation.

Conversely, the reference watersheds did not observe the same long-term trends in PM AET (Figure 15). The year 2001 was omitted in Figure 15 because of erroneous numbers and to retain the integrity of the remaining data. No trends were observed in Fausett Creek or Falling Creek ($\tau b = -0.205$, $p= 0.110$; $\tau b = -0.064$, $p= 0.350$, respectively) watersheds' AET or meteorologic parameters controlling AET, namely solar radiation. While solar radiation didn't have a significant trend in Fausett Creek watershed ($\tau b = -0.216$, $p= 0.098$) or Falling Creek watershed ($\tau b = -0.064$, $p= 0.350$), it was clearly a major cause of the declining AET in the

SRW. It was also found that solar radiation does account for approximately 66% of the variance in AET at both watersheds.

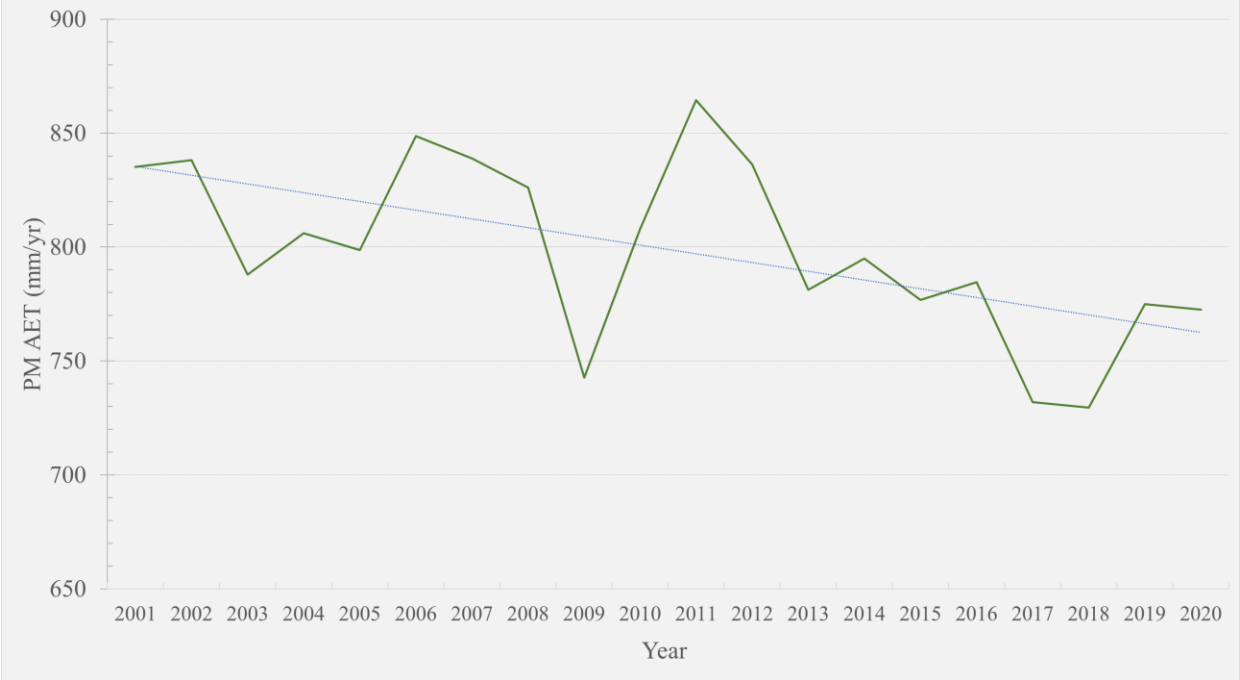

Figure 14: Annual estimates of PM AET within the SRW from 2001-2020 including the surface water availability procedure (p=0.002).

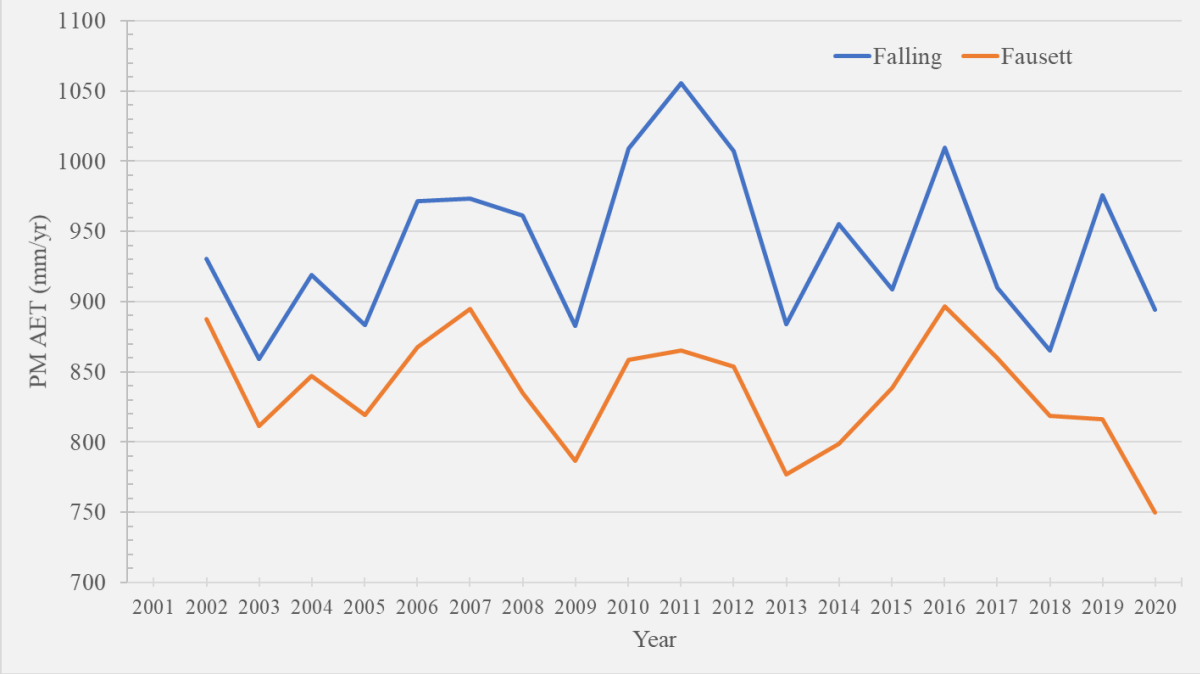

Figure 15: Annual estimates of PM AET within each reference watershed from 2002-2020 including the surface water availability procedure (Falling p=0.350; Fausett p=0.098).

3.3.1 Sensitivity Analysis

The sensitivity analysis reveals that incoming solar radiation has the largest effect on AET in all land cover types (Figure 16). The sensitivity analysis supports findings in Figures 6 and 14; where solar radiation seems to be the most important driver of AET. Wind speed had the smallest effect of the final PM estimates in each land cover type. Across all land cover types, mixed forest seems to be the most responsive to change in any variable. Conversely, high intensity developed land showed the least amount of change with adjustment for all meteorologic parameters. Full records of the sensitivity analysis results can be found in Appendix G.

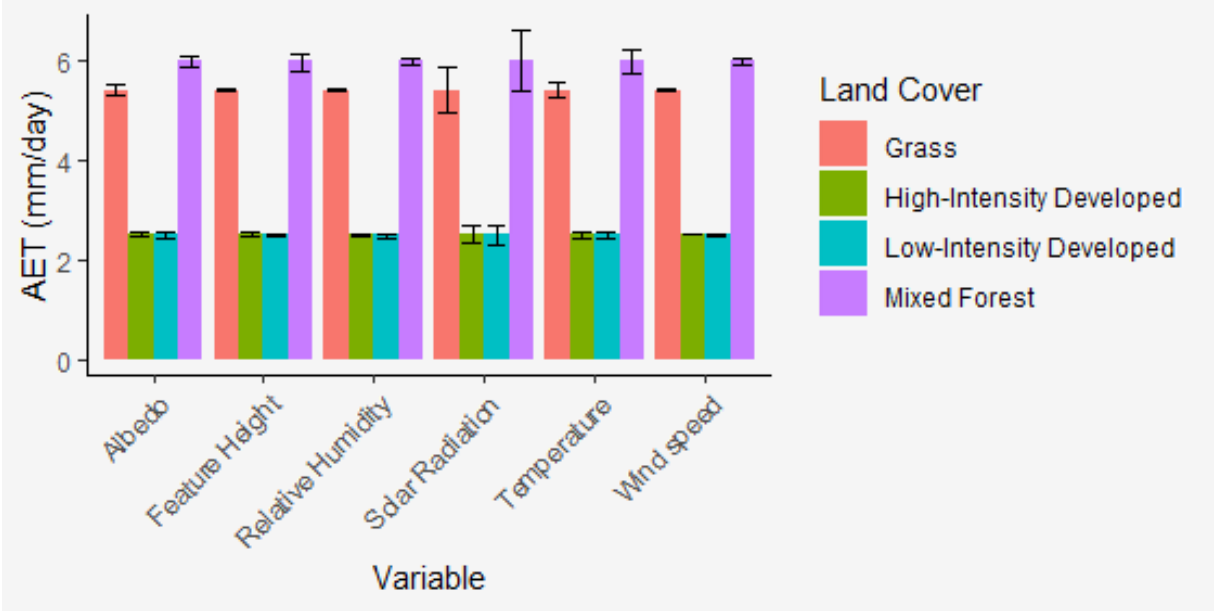

Figure 16: Daily AET before areal weighting and surface water availability model. Visualization of adjusting six variables (albedo, feature height, relative humidity, solar radiation, temperature, and wind speed) up by 10% and down by 10% on the day with highest ET in entire study (J=168, June 17, 2001) within four land cover types. Bars show the original value, while the error line depict the AET when variables are adjusted (one at a time).

3.4 Model Comparisons

Falling Creek watershed had an average annual AET of 948.20 mm/yr, whereas Fausett Creek watershed exhibited an average annual AET of 925.13 mm/yr (Table 11). Comparing the

regression models and the PM AET approach with the water balance AET of reference watersheds revealed the results found in Figure 17, where deviations from the water balance 'reference' AET are displayed. Remotely sensed TerraClimate datasets consistently overestimate AET given the positive bars above zero in both watersheds. In both reference watersheds, the PM approach returned estimates that were the closest to the water balance AET with estimates of 960.89 mm/yr in Falling Creek watershed and 855.4 mm/yr in Fausett Creek watershed. The Fang Type I-Lumped model performs similarly to the PM AET approach, returning an estimate of 921.63 mm/yr in Falling Creek watershed and 852.57 mm/yr in Fausett Creek watershed. As seen by the negative bars in Figure 17, the remaining models largely underestimate AET within the undeveloped watersheds. PM underestimates AET at both watersheds, with a much larger underestimate at Fausett Creek.

Table 11: Average annual precipitation and stream discharge from 2001—2020 for reference watersheds: Falling Creek and Fausett Creek. Annual AET is calculated by subtracting discharge from precipitation.

Watershed	Precipitation (mm/yr)	Discharge (mm/yr)	AET (mm/yr)
Falling Creek	1184.65	236.46	948.20
Fausett Creek	1446.68	521.55	925.13

Figure 17: (a) Falling Creek models' deviation from water balance AET of 948.20 mm/yr, and (b) Fausett Creek models' deviation from the water balance AET of 925.13 mm/yr.

The SRW AET model estimates show considerable variation, returning estimates ranging from as low as 600 mm/yr to 1000 mm/yr (Figure 18). Before scaling SRW estimates for possible underestimation, it can be observed that the PM approach was the second highest model estimate after Fang Type II Lumped model. While there is not a definite way to validate the TerraClimate dataset within the SRW, it can be assumed that it overestimates watershed AET once again, as the SRW estimate is just as high as or higher than reference, undeveloped watershed TerraClimate estimates. After scaling, TerraClimate AET was reduced to 916.83 mm/yr, whereas every other model saw an increase in the long-term annual estimate. Models' annual AET estimates before and after applying the scaling factor can be found in Table 12. The standard deviation of the PM model is also shown in Table 12, and because the regression models do not estimate AET continuously, a SD cannot be calculated. After the scaling factors

were applied to long-term annual PM estimates, the adjusted annual AET estimate for the SRW is 826.03 mm/yr.

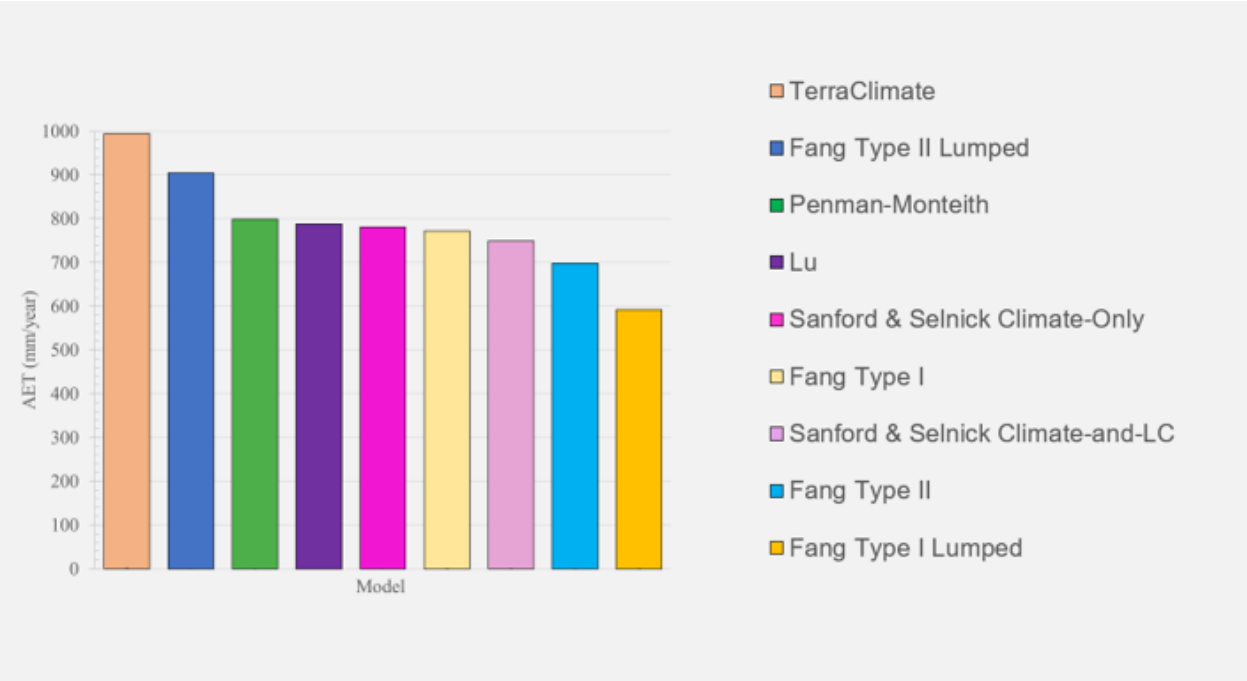

Figure 18: SRW mean annual AET of all models from 2001-2020.

Table 12: SRW long-term annual AET computed by each model with reference watershed scaling ratios and adjusted SRW AET. Reference watershed scaling ratios were calculated by dividing calculated water balance AET by the respective model AET.

Model	SRW ET (mm/yr)	Standard Deviation (mm/yr)	Average Scaling Ratio (Fasuett and Falling Watersheds; Water Balance ET/Model ET)	Adjusted SRW ET (mm/yr)
TerraClimate	994.50	-	0.92	916.63
Fang Type II Lumped	904.41	-	1.12	1009.75
Penman-Monteith	798.91	37.66	1.03	826.03
Lu	788.33	-	1.11	877.25
Sanford & Selnick Climate-Only	780.96	-	1.17	910.21
Fang Type I	771.92	-	1.08	831.67
Sanford & Selnick Climate-and-LC	749.32	-	1.18	882.79
Fang Type II	697.96	-	1.19	829.58
Fang Type I Lumped	592.01	-	1.06	625.62

4 DISCUSSION

4.1 Land cover analysis confirms the composition of developed NLCD classes

The results of the land cover analysis procedure confirm that the NLCD composition of developed classes are accurate. The definitions of each developed class provided by the NLCD confirm that the land cover class compositions revealed in this study are accurate and representative of the actual land cover in the SRW. ‘Developed, Open Space’ areas are a mixture of some built surfaces, but mostly vegetation, where impervious surfaces account for less than 20% of total cover. ‘Developed, Low Intensity’, ‘Developed, Medium Intensity’, and ‘Developed High Intensity’ classes contain 20%-49%, 50%-79%, and 80%-100% of impervious cover, respectively.

Based on the reviewed body of literature to estimate urban watershed AET, this study’s land cover analysis is the most intensive method observed because of the validation and correction of mixed pixel data from NLCD. Grimmond and Oke (1986) partitioned total land cover into impervious and pervious land cover, where 30% of the pervious cover was irrigated, and each land cover type required different coefficients for AET equations. Bhaskar and Welty (2012) only analyzed percent imperviousness within each analyzed watershed. The more arid climate of Los Angeles, California in Litvak et al. (2017) analyzed impervious, trees (gymnosperm, angiosperm, palms), irrigated turfgrass, bare soil, where all vegetated cover AET was calculated with different regression models dependent on plant type, and AET of non-vegetative cover was considered negligible. Other studies address multiple types of land covers like forest, grass, urban and agricultural lands, but the satellite data acquired with a course resolution remains unadjusted for mixed pixel issues (Gyamfi et al., 2016; Jia et al., 2001; Q. Wang et al., 2020).

4.2 Penman-Monteith approach shows AET is decreasing in a suburbanized watershed

The PM AET results illuminated by this study are comparable to results in previously published literature. Bhaskar and Welty (2012) conducted a study in Baltimore, Maryland where the climate is also considered to be a humid subtropical climate. Their study analyzed many watersheds with varying degrees of imperviousness, where rural watersheds had a water budget AET of 830 mm/yr and urban watersheds had an water budget AET of 360 mm/yr; however, the urbanized watersheds in that study were much more urbanized than the SRW. Irrigation was estimated by a different procedure, where 25% of the area classified as grass/scrub is irrigated at a rate of 1 in. (25.4 mm) per week for 4 months of the year (Claessens et al., 2006; Milesi et al., 2005). The SRW summer daily AET estimate of 5.12-5.24 mm/day also aligns with the results of Grimmond and Oke (1986), where they estimated the summer daily AET was 5-6 mm/day; however, the annual AET of 578 mm/yr in Grimmond and Oke (1986) is much lower than the SRW annual average because of Vancouver's moderate, oceanic climate (Cfb Köppen climate classification). Another study analyzed AET in the highly urbanized 64-square mile Wissahickon Creek watershed, Pennsylvania, USA, where average annual AET, calculated by water budgets, was estimated to be 587.25 mm/yr (Sloto & Buxton, 2005), but land cover types are not addressed by their methods. Additionally, AET was found to be 612.90 mm/yr by water budgets in the urbanized Cooper River watershed in New Jersey (Sloto & Buxton, 2005), but again it is hard to know the accuracy of these methods because they do not account for different land surfaces.

The percent difference between the reference watershed average 'observed' AET and the PM SRW AET is -17.2%, where the SRW experiences lower AET than undisturbed watersheds. Because the annual SRW AET is comparable to other results within another undeveloped,

Piedmont region (887.5 mm/yr, (Aulenbach & Peters, 2018)), our results could point to the importance of our land cover analysis procedure. During the land cover data collection stage, if trees were covering impervious land cover, the land cover was still considered forested. The annual AET observed in undeveloped Piedmont watersheds support the idea even when there is developed land cover beneath tree canopies the vegetative cover is the land cover that interacts with the atmosphere in AET processes.

SRW has much more vegetation than other urban watersheds where AET has been calculated. The original contribution of impervious AET to total AET was 16.8% before the surface water availability model and 9.8% following the surface water availability model. Although the SRW is considered a true suburban watershed, this contribution is much less than previously published work, where the contribution of developed AET ranges from 17%-29% (Cohard et al., 2018; Ragab et al., 2003; Zhou et al., 2021). If the entire SRW was converted to impervious land cover, the long-term annual average of AET would be 77.87 mm/yr. This can lead us to infer that if an entire watershed was developed upon within a humid subtropical climate, total annual AET could be reduced to roughly a tenth of the original value. While the reviewed urban AET studies have a variety of heterogeneous land cover compositions, the SRW is still roughly 72% vegetated, supporting the conclusion that AET will remain higher than many other urban AET studies unless drastic land cover composition changes are made (Claessens et al., 2006; Grimmond & Oke, 1991; Gyamfi et al., 2016; Kokkonen et al., 2018; Mitchell et al., 2008; Q. Wang et al., 2020).

4.2.1 Decreasing AET is driven by increasing impervious cover and decreasing solar radiation

The interannual variability of AET within the SRW could be explained by land cover change and/or long-term changes is meteorological parameters. Throughout the entire study period, there is a decrease in annual AET of 3.12 mm/yr, 0.39% of the long-term annual average (Figure 14). Kokkonen et al. (2018) similarly observed a decrease in long-term annual AET of 1.3 mm/yr (roughly 0.43% of the total annual AET with realistic irrigation scenarios), but the authors indicate that this estimate was offset by local irrigation practices. While the amount of precipitation is relatively unchanged throughout the study period, a general trend of increasing incoming solar radiation has occurred in North America since 2000 (M. Yuan et al., 2021). The increases in incoming solar radiation can lead to greater vapor pressure deficits and lower overall relative humidity when compared to nearby rural areas, particularly in humid regions (Hao et al., 2018), leading to exacerbated urban dry island (UDI) effects. Based on Figure 7, the observed increasing global incoming solar radiation trend is not reflected in the SRW.

The long-term decrease in annual AET within the SRW can be attributed to an 8.6% increase in developed land cover, a 4.3% decrease in total forest cover, and the decreasing incoming solar energy that fuels AET processes, which is supported by our sensitivity analysis and the fact that the PM model is mostly energy determined (Mao & Wang, 2017). The solar radiation is confirmed to be correlated to the annual PM AET estimates, and therefore responsible for the AET long-term trend (Figure 19). Aulenbach and Peters (2018) observed little interannual variability in AET in the forested Panola Mountain watershed, and the coefficient of variation of their estimates is 13.2%. Similarly, Oishi et al. (2010) saw little interannual variability in annual AET of the Duke Forest in North Carolina, and the coefficient of variation

for their estimates is 4.1%, slightly lower than the SRW PM coefficient of variation (4.7%). The lack of PM AET interannual variability in Falling Creek watershed and Fausett Creek watershed in this study support the Aulenbach and Peters (2018) and Oishi et al. (2010) findings where undeveloped regions observe little interannual variability. Impervious surfaces in urban environments have marginal water storage capacity, and AET quickly trends toward zero following precipitation events. The transient nature of evaporation from these surfaces is suggestive that the temporal variability of AET in urban/suburban watersheds would be greater than in completely vegetated watersheds. One of the most important findings, however, is this urban/suburban watershed is even more forested than the unaltered NLCD land-cover data would suggest. The impact of impervious surfaces on AET, and its variability, was surprisingly marginal.

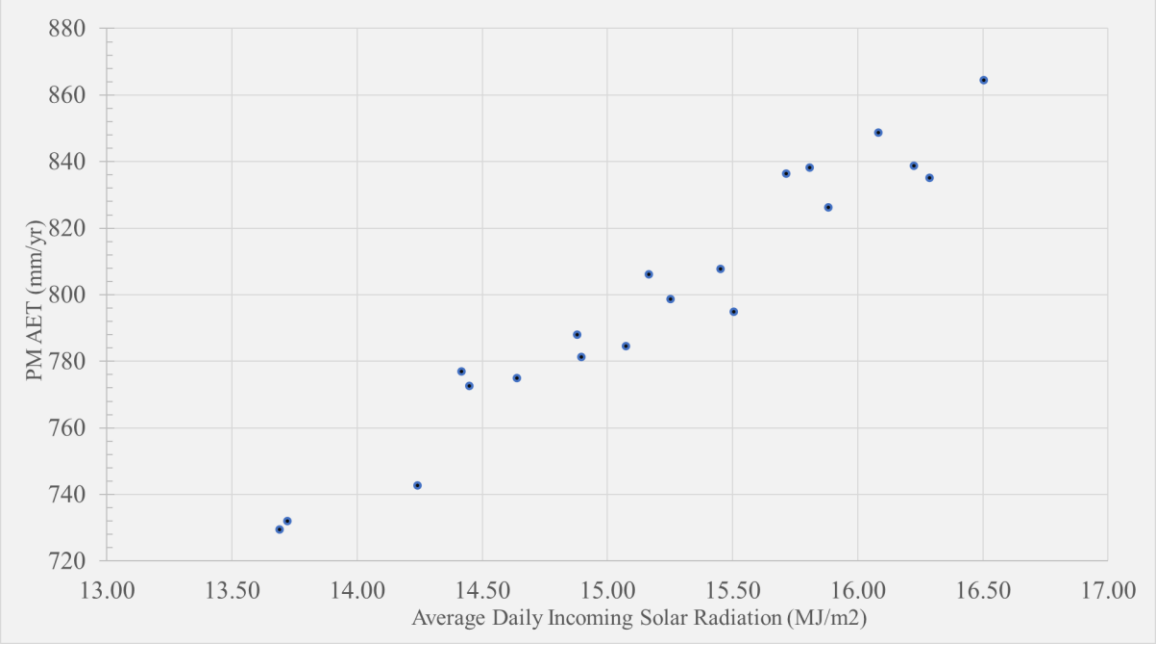

Figure 19: Scatter plot of average daily incoming solar radiation by year and average annual PM AET estimates.

Many uncertainties are associated with PM AET modelling. Firstly, the chosen PM submodels could have varying impacts on the accuracy of final AET estimates, especially the net

radiation net radiation and resistance parameters. The sensitivity of the PM approach to incoming solar radiation could be explained by the utilization of solar radiation data within so many of the PM submodels, highlighting its importance in modeling AET. Incoming solar radiation data are used to calculate three of the nine variables within the PM equation: net radiation, storage heat flux, and surface resistance. Therefore, any changes in incoming solar radiation propagate throughout the PM AET process. The surface water availability submodel and the water-storage capacity of impervious surfaces are also poorly constrained by observations and data. The temporal resolution at which the PM equation is used can have a large impact on accuracy of AET estimates. Longer temporal scales can dismiss important fluctuations in meteorological variables that would impact AET rates, such as diurnal patterns in solar radiation, temperature, wind speed, and vapor pressure. The PM model also does not consider the vegetation physiological impacts of elevated atmospheric CO_2 concentrations on AET. The trends of global warming and concentration of atmospheric CO_2 have been proven to have effects on vegetation transpiration rates (Kirschbaum & McMillan, 2018). The fact remains that the PM model alone does not address water availability within a watershed, so failing to complete the water availability storage procedure can overestimate AET.

Evaporation from impervious surfaces is likely underestimated in this study. The evaporation from impervious services in the SRW is about 6% annually (ET_{imp}/Precip), which is considerably lower than previously published field studies. The range of published evaporation rates range from as low as 16% in one location and as much as 29% in another (Zhao et al., 2021). Other papers report 21-24% (Ragab et al., 2003), 19% (Davies, 1981), and 17% (Cohard et al., 2018).

4.3 Model Comparisons

The regression models' results were generally unpredictable and varying degrees of accuracy when compared to water balance AET. Within the reference watersheds, the Fang Type I-Lumped model performs similarly to the PM AET approach, returning an estimate of 921.63 mm/yr in Falling Creek watershed and 852.57 mm/yr in Fausett Creek watershed. This leads us to believe that the Fang Type I-Lumped regression model could be useful in undeveloped watersheds. In all of the Fang models, the 19% fraction used to estimate AET from impervious surfaces could have been an underestimate, meaning the AET calculated by these models are underestimated as well. One study conducted in France measured that 30-40% of precipitation is evaporated when it falls on impervious surfaces (Ramier et al., 2011), so the estimates from the Fang models may be artificially low. The remaining regression models consistently underestimate watershed AET compared to PM, which could be for a few reasons. The most relevant answer could be that the water balance approach overestimates AET in the two reference watersheds. The water balance approach makes assumptions about where water travels within a watershed. Water flowing to a single outlet point can take many paths, not just through the stream channels where gauges are found. Studies have found that water balance approaches to estimate AET can be improved by adequately modelling subsurface water movement, as fractured bedrock formations can promote increase groundwater seepage (Fan, 2019; Graham et al., 2010; Kampf et al., 2020; Safeeq et al., 2021). Additionally, errors in watershed water balance approaches increase as basin size increases due to more variation and uncertainty in runoff generation, storage areas, and saturated zone connectivity (McGlynn et al., 2004).

Impervious land covers are neglected in all of the regression models except for the Sanford and Selnick (2015) land-cover-and-climate model, limiting their applicability in

urbanized watersheds. The Sanford and Selnick model returns an annual SRW AET estimate of 706.18 mm/yr in a completely impervious watershed. Alternatively, the Lu model would return a an annual SRW AET of 701.70 mm/yr because all that changes in the model is the percentage of forest cover, not meteorological variables. If the entire SRW was impervious land cover in the remaining regression models, the AET would have to be calculated using the published proportional values of precipitation lost to evaporation. Using the 19% precipitation to evaporation estimate utilized previously in the Fang models, the SRW AET would be 255.86 mm/yr in completely impervious, contrasting with the 77.87 mm/yr AET estimate returned by the PM model after accounting for surface water availability. The 19% estimate used in conjunction with statistical models would be considered an overestimate if compared to the results from the PM approach. The variability in the AET estimates for a completely impervious watershed leads us to believe that these regression models were not entirely suitable for urbanized catchments, and if the 19% estimate was reduced to the estimate found in the SRW (9.8%) the statistical models may underestimate AET even more than previously calculated.

5 CONCLUSIONS

Many novel conclusions can be made from this research endeavor. Not only were new workflows created to accurately model PM equation parameters and validate land cover data, but the results of these workflows also support many inferences.

1. Firstly, manual land cover analysis revealed considerable heterogeneity within each of the NLCD developed LC classes. Developed classes (developed open space, low-intensity developed, medium-intensity developed, and high-intensity developed) had 48.18%, 24.26%, 13.79%, and 4.43% forest cover, respectively.
2. Secondly, based on results from the PM model, the annual AET in the SRW is roughly 800 mm/yr while undeveloped Falling Creek watershed and Fausett Creek watershed nearby observed PM AET estimates of 960.38 mm/yr and 855.12 mm/yr, respectively. In addition to being more physically based to include surface-specific characteristics, the PM approach also showed closest agreement with water balance calculations in reference watersheds. In the humid subtropical climate of the study area, SRW summer AET was roughly three times larger than winter estimates, and annual AET showed a declining trend over two decades, most likely due to decreasing solar radiation and a small increase in the percentage of developed land cover. It was found that the over the study period, there was a 10% reduction in total annual AET, supporting the fact that long-term interannual variability exists in urban watersheds, unlike undisturbed, vegetated watersheds. Within the Piedmont region, this semi-urbanized watershed exhibited more interannual variability than was observed by completely forested areas. This means that the AET in urban watersheds are more sensitive to climatic changes. We also found that impervious surfaces are a

small but not-negligible contributor to AET in urban areas, accounting for about 9.8% of total urban AET within the SRW annually.

3. Third, the statistical approaches underestimate AET in undeveloped watersheds, while TerraClimate datasets overestimate watershed AET, especially in urban watersheds.

In future research, AET in humid subtropical watersheds with higher degrees of urbanization than the SRW could be investigated. The SRW is considered suburban by the USGS, so the implications to AET in more urbanized study areas are limited. Additionally, although hard to find and successfully utilize, improved AET datasets to validate results could be used. If these data products do not exist in the desired study area, research and development of accurate AET acquisition could be a worthwhile task. Future research is also needed to better understand the role of groundwater and urban structural additions like leaky pipe networks and water treatment/sewer treatment facilities have on urban AET. To accurately measure effect on AET from anthropogenic water inputs like irrigation, more surveys or community-based outreach could be done to better represent local household water use practices.

REFERENCES

Abatzoglou, J. T., Dobrowski, S. Z., Parks, S. A., & Hegewisch, K. C. (2018). TerraClimate, a high-resolution global dataset of monthly climate and climatic water balance from 1958–2015. *Scientific Data*, *5*(1), 170191. https://doi.org/10.1038/sdata.2017.191

Abdullah, A. Y. M., Masrur, A., Adnan, M. S. G., Baky, Md. A. A., Hassan, Q. K., & Dewan, A. (2019). Spatio-temporal Patterns of Land Use/Land Cover Change in the Heterogeneous Coastal Region of Bangladesh between 1990 and 2017. *Remote Sensing*, *11*(7), 790. https://doi.org/10.3390/rs11070790

Allen, R. G., Pereira, L. S., Raes, D., & Smith, M. (1998). *Crop evapotranspiration—Guidelines for computing crop water requirements—FAO Irrigation and drainage paper 56*. 15.

Aminzadeh, M., & Or, D. (2017). The complementary relationship between actual and potential evaporation for spatially heterogeneous surfaces: CR FOR SPATIALLY HETEROGENEOUS SURFACES. *Water Resources Research*, *53*(1), 580–601. https://doi.org/10.1002/2016WR019759

An, N., Hemmati, S., & Cui, Y.-J. (2017). Assessment of the methods for determining net radiation at different time-scales of meteorological variables. *Journal of Rock Mechanics and Geotechnical Engineering*, *9*(2), 239–246. https://doi.org/10.1016/j.jrmge.2016.10.004

Aulenbach, B. T., & Peters, N. E. (2018). Quantifying Climate-Related Interactions in Shallow and Deep Storage and Evapotranspiration in a Forested, Seasonally Water-Limited Watershed in the Southeastern United States. *Water Resources Research*, *54*(4), 3037–3061. https://doi.org/10.1002/2017WR020964

Baldocchi, D., Falge, E., Gu, L., Olson, R., Hollinger, D., Running, S., Anthoni, P., Bernhofer, C., Davis, K., Evans, R., Fuentes, J., Goldstein, A., Katul, G., Law, B., Lee, X., Malhi, Y., Meyers, T., Munger, W., Oechel, W., … Wofsy, S. (2001). FLUXNET: A New Tool to Study the Temporal and Spatial Variability of Ecosystem-Scale Carbon Dioxide, Water Vapor, and Energy Flux Densities. *Bulletin of the American Meteorological Society*, *82*(11), 21.

Baldocchi, D., Finnigan, J., Wilson, K., Paw U, K. T., & Falge, E. (2000). On Measuring Net Ecosystem Carbon Exchange Over Tall Vegetation on Complex Terrain. *Boundary-Layer Meteorology*, *96*(1–2), 257–291. https://doi.org/10.1023/A:1002497616547

Barcza, Z., Kern, A., Haszpra, L., & Kljun, N. (2009). Spatial representativeness of tall tower eddy covariance measurements using remote sensing and footprint analysis. *Agricultural and Forest Meteorology*, *149*(5), 795–807. https://doi.org/10.1016/j.agrformet.2008.10.021

Barnes, C. A., & Roy, D. P. (2010). Radiative forcing over the conterminous United States due to contemporary land cover land use change and sensitivity to snow and interannual

albedo variability. *Journal of Geophysical Research*, *115*(G4), G04033. https://doi.org/10.1029/2010JG001428

Belda, M., Holtanová, E., Halenka, T., & Kalvová, J. (2014). Climate classification revisited: From Köppen to Trewartha. *Climate Research*, *59*(1), 1–13. https://doi.org/10.3354/cr01204

Bhaskar, A. S., Beesley, L., Burns, M. J., Fletcher, T. D., Hamel, P., Oldham, C. E., & Roy, A. H. (2016). *Will it rise or will it fall? Managing the complex effects of urbanization on base flow*. 19.

Bhaskar, A. S., Hogan, D. M., & Archfield, S. A. (2016). Urban base flow with low impact development. *Hydrological Processes*, *30*(18), 3156–3171. https://doi.org/10.1002/hyp.10808

Bhaskar, A. S., & Welty, C. (2012). Water Balances along an Urban-to-Rural Gradient of Metropolitan Baltimore, 2001-2009. *Environmental & Engineering Geoscience*, *18*(1), 37–50. https://doi.org/10.2113/gseegeosci.18.1.37

Boegh, E., Soegaard, H., & Thomsen, A. (2002). Evaluating evapotranspiration rates and surface conditions using Landsat TM to estimate atmospheric resistance and surface resistance. *Remote Sensing of Environment*, *79*(2–3), 329–343. https://doi.org/10.1016/S0034-4257(01)00283-8

Brest, C. L. (1987). Seasonal Albedo of an Urban/Rural Landscape from Satellite Observations. *Journal of Applied Meteorology and Climatology*, *26*, 1169–1187.

Brutsaert, W. (2005). *Hydrology: An Introduction*. Cambridge University Press; Cambridge Core. https://doi.org/10.1017/CBO9780511808470

Buban, M. S., Lee, T. R., & Baker, C. B. (2020). A Comparison of the U.S. Climate Reference Network Precipitation Data to the Parameter-Elevation Regressions on Independent Slopes Model (PRISM). *Journal of Hydrometeorology*, *21*(10), 2391–2400. https://doi.org/10.1175/JHM-D-19-0232.1

Changnon, S. A., Huff, F. A., & Semonin, R. G. (1971). *METROMEX: an investigation ot inadvertent weather modification*. *52*(10), 11.

Choi, M., Kustas, W. P., & Ray, R. L. (2012). Evapotranspiration models of different complexity for multiple land cover types: EVAPOTRANSPIRATION MODELS FOR MULTIPLE LAND COVER TYPES. *Hydrological Processes*, *26*(19), 2962–2972. https://doi.org/10.1002/hyp.8346

Claessens, L., Hopkinson, C., Rastetter, E., & Vallino, J. (2006). Effect of historical changes in land use and climate on the water budget of an urbanizing watershed: LAND USE AND CLIMATE EFFECTS ON WATER BUDGET. *Water Resources Research*, *42*(3). https://doi.org/10.1029/2005WR004131

Cohard, J.-M., Rosant, J.-M., Rodriguez, F., Andrieu, H., Mestayer, P. G., & Guillevic, P. (2018). Energy and water budgets of asphalt concrete pavement under simulated rain events. *Urban Climate*, *24*, 675–691. https://doi.org/10.1016/j.uclim.2017.08.009

Collier, P., & Venables, A. J. (2016). Urban infrastructure for development. *Oxford Review of Economic Policy*, *32*(3), 391–409. https://doi.org/10.1093/oxrep/grw016

Davies, H. A. (1981). *THE WATER BALANCE OF URBAN IMPERMIABLE SURFACES: CATCHMENT AND PROCESS STUDIES*. University College London.

Diem, J. E. (2007). Detecting summer rainfall enhancement within metropolitan Atlanta, Georgia USA. *International Journal of Climatology*, *28*(1), 129–133. https://doi.org/10.1002/joc.1560

Dingman, S. L. (2002). *Physical Hydrology* (2nd Edition). Pearson.

Diouf, O. C., Weihermüller, L., Ba, K., Cisse Faye, S., Faye, S., & Vereecken, H. (2016). Estimation of Turc reference evapotranspiration with limited data against the Penman-Monteith Formula in Senegal. *Journal of Agriculture and Environment for International Development (JAEID)*, *110*(1). https://doi.org/10.12895/jaeid.20161.417

Eagleman, J. R. (1967). *Pan Evaporation, Potential and Actual Evapotranspiration*. *6*, 7.

Famiglietti, J. S., & Wood, E. F. (1995). Effects of Spatial Variability and Scale on Areally Averaged Evapotranspiration. *Water Resources Research*, *31*(3), 699–712. https://doi.org/10.1029/94WR02820

Fan, Y. (2019). Are catchments leaky? *WIREs Water*, *6*(6). https://doi.org/10.1002/wat2.1386

Fang, B., Lei, H., Zhang, Y., Quan, Q., & Yang, D. (2020). Spatio-temporal patterns of evapotranspiration based on upscaling eddy covariance measurements in the dryland of the North China Plain. *Agricultural and Forest Meteorology*, *281*, 107844. https://doi.org/10.1016/j.agrformet.2019.107844

Fang, Hao, L., Cao, Z., Huang, X., Qin, M., Hu, J., Liu, Y., & Sun, G. (2020). Combined effects of urbanization and climate change on watershed evapotranspiration at multiple spatial scales. *Journal of Hydrology*, *587*, 124869. https://doi.org/10.1016/j.jhydrol.2020.124869

Fang, Y., Sun, G., Caldwell, P., McNulty, S. G., Noormets, A., Domec, J.-C., King, J., Zhang, Z., Zhang, X., Lin, G., Zhou, G., Xiao, J., & Chen, J. (2016b). Monthly land cover-specific evapotranspiration models derived from global eddy flux measurements and remote sensing data: Monthly ET Models. *Ecohydrology*, *9*(2), 248–266. https://doi.org/10.1002/eco.1629

Fatichi, S., & Ivanov, V. Y. (2014). Interannual variability of evapotranspiration and vegetation productivity. *Water Resources Research*, *50*(4), 3275–3294. https://doi.org/10.1002/2013WR015044

Fisher, J. B., Whittaker, R. J., & Malhi, Y. (2011). ET come home: Potential evapotranspiration in geographical ecology: ET come home. *Global Ecology and Biogeography*, *20*(1), 1–18. https://doi.org/10.1111/j.1466-8238.2010.00578.x

Gao, X., Gu, F., Gong, D., Hao, W., Chu, J., & Li, H. (2020). Comparison of three evapotranspiration models in a rain-fed spring maize filed in the Loess Plateau, China. *Journal of Agricultural Meteorology*, *76*(4), 155–163. https://doi.org/10.2480/agrmet.D-20-00010

Göckede, M., Rebmann, C., & Foken, T. (2004). A combination of quality assessment tools for eddy covariance measurements with footprint modelling for the characterisation of complex sites. *Agricultural and Forest Meteorology*, *127*(3–4), 175–188. https://doi.org/10.1016/j.agrformet.2004.07.012

Graham, C. B., Woods, R. A., & McDonnell, J. J. (2010). Hillslope threshold response to rainfall: (1) A field based forensic approach. *Journal of Hydrology*, *393*(1–2), 65–76. https://doi.org/10.1016/j.jhydrol.2009.12.015

Grimmond, C. S. B., & Oke, T. R. (1986). Urban Water Balance: 2. Results From a Suburb of Vancouver, British Columbia. *Water Resources Research*, *22*(10), 1404–1412. https://doi.org/10.1029/WR022i010p01404

Grimmond, C. S. B., & Oke, T. R. (1991). An evapotranspiration-interception model for urban areas. *Water Resources Research*, *27*(7), 1739–1755. https://doi.org/10.1029/91WR00557

Grimmond, C. S. B., & Oke, T. R. (1999). Heat Storage in Urban Areas: Local-Scale Observations and Evaluation of a Simple Model. *JOURNAL OF APPLIED METEOROLOGY*, *38*, 19.

Grimmond, C. S. B., & Oke, T. R. (2002). Turbulent Heat Fluxes in Urban Areas: Observations and a Local-Scale Urban Meteorological Parameterization Scheme (LUMPS). *JOURNAL OF APPLIED METEOROLOGY*, *41*, 19.

Grimmond, C. S. B., Oke, T. R., & Steyn, D. G. (1986). Urban Water Balance: 1. A Model for Daily Totals. *Water Resources Research*, *22*(10), 1397–1403. https://doi.org/10.1029/WR022i010p01397

Gyamfi, C., Ndambuki, J. M., & Salim, R. W. (2016). *Hydrological Responses to Land Use/Cover Changes in the Olifants Basin, South Africa*. 16.

Hamilton, S. K., Hussain, M. Z., Lowrie, C., Basso, B., & Robertson, G. P. (2018). Evapotranspiration is resilient in the face of land cover and climate change in a humid temperate catchment. *Hydrological Processes*, *32*(5), 655–663. https://doi.org/10.1002/hyp.11447

Hao, L., Huang, X., Qin, M., Liu, Y., Li, W., & Sun, G. (2018). Ecohydrological Processes Explain Urban Dry Island Effects in a Wet Region, Southern China. *Water Resources Research*, 15.

Healy, R. W., Winter, T. C., LaBaugh, J. W., & Franke, O. L. (2007). *Circular* (Water Budgets: Foundations for Effective Water-Resources and Environmental Management) [Circular]. USGS.

Helsel, D. R., & Hirsch, R. M. (2002). *Techniques of Water-Resources Investigations of the United States Geological Survey: Book 4, Hydrologic Analysis and Interpretation*. United States Geological Survery.

Hill, T., Chocholek, M., & Clement, R. (2017). The case for increasing the statistical power of eddy covariance ecosystem studies: Why, where and how? *Global Change Biology*, *23*(6), 2154–2165. https://doi.org/10.1111/gcb.13547

Hogan, P., Parajka, J., Oismüller, M., Heng, L., Strauss, P., & Blöschl, G. (2020). High-Frequency Stable-Isotope Measurements of Evapotranspiration Partitioning in a Maize Field. *Water*, *12*(11), 3048. https://doi.org/10.3390/w12113048

Hollis, G. E. (1988). *Rain, Roads, Roofs and Runoff: Hydrology in Cities*. 11.

Hopkins, K. G., Morse, N. B., Bain, D. J., Bettez, N. D., Grimm, N. B., Morse, J. L., & Palta, M. M. (2015). *Type and timing of stream f low changes in urbanizing watersheds in the Eastern U.S.* 14.

Hwang, R.-L., Lin, T.-P., & Matzarakis, A. (2011). Seasonal effects of urban street shading on long-term outdoor thermal comfort. *Building and Environment*, *46*(4), 863–870. https://doi.org/10.1016/j.buildenv.2010.10.017

Järvi, L., Grimmond, C. S. B., & Christen, A. (2011). The Surface Urban Energy and Water Balance Scheme (SUEWS): Evaluation in Los Angeles and Vancouver. *Journal of Hydrology*, *411*(3–4), 219–237. https://doi.org/10.1016/j.jhydrol.2011.10.001

Jarvi, P. G. (1976). The interpretation of the variations in leaf water potential and stomatal conductance found in canopies in the field. *Philosophical Transactions of the Royal Society of London. B, Biological Sciences*, *273*(927), 593–610. https://doi.org/10.1098/rstb.1976.0035

Jia, Y., Ni, G., Kawahara, Y., & Suetsugi, T. (2001). Development of WEP model and its application to an urban watershed. *Hydrological Processes*, *15*(11), 2175–2194. https://doi.org/10.1002/hyp.275

Kampf, S. K., Burges, S. J., Hammond, J. C., Bhaskar, A., Covino, T. P., Eurich, A., Harrison, H., Lefsky, M., Martin, C., McGrath, D., Puntenney-Desmond, K., & Willi, K. (2020). The Case for an Open Water Balance: Re-envisioning Network Design and Data Analysis for a Complex, Uncertain World. *Water Resources Research*, *56*(6). https://doi.org/10.1029/2019WR026699

Kastner-Klein, P., Berkowicz, R., & Britter, R. (2004). The influence of street architecture on flow and dispersion in street canyons. *Meteorology and Atmospheric Physics*, *87*(1–3). https://doi.org/10.1007/s00703-003-0065-4

Kaushal, S. S., & Belt, K. T. (2012). The urban watershed continuum: Evolving spatial and temporal dimensions. *Urban Ecosyst*, 27.

Kirschbaum, M. U. F., & McMillan, A. M. S. (2018). Warming and Elevated CO2 Have Opposing Influences on Transpiration. Which is more Important? *Current Forestry Reports*, *4*(2), 51–71. https://doi.org/10.1007/s40725-018-0073-8

Kokkonen, T. V., Grimmond, C. S. B., Christen, A., Oke, T. R., & Järvi, L. (2018). Changes to the Water Balance Over a Century of Urban Development in Two Neighborhoods: Vancouver, Canada. *Water Resources Research*, *54*(9), 6625–6642. https://doi.org/10.1029/2017WR022445

Litvak, E., Manago, K. F., Hogue, T. S., & Pataki, D. E. (2017). Evapotranspiration of urban landscapes in Los Angeles, California at the municipal scale: EVAPOTRANSPIRATION OF URBAN LANDSCAPES. *Water Resources Research*, *53*(5), 4236–4252. https://doi.org/10.1002/2016WR020254

Liu, J., & Niyogi, D. (2019). Meta-analysis of urbanization impact on rainfall modification. *Scientific Reports*, *9*(1), 7301. https://doi.org/10.1038/s41598-019-42494-2

Liu, S., Mao, D., & Lu, L. (2006). *Measurement and estimation of the aerodynamic resistance* [Preprint]. https://doi.org/10.5194/hessd-3-681-2006

Lu, J., Sun, G., McNulty, S. G., & Amatya, D. M. (2003). MODELING ACTUAL EVAPOTRANSPIRATION FROM FORESTED WATERSHEDS ACROSS THE SOUTHEASTERN UNITED STATES. *Journal of the American Water Resources Association*, *39*(4), 886–896. https://doi.org/10.1111/j.1752-1688.2003.tb04413.x

Lu, J., Sun, G., McNulty, S. G., & Amatya, D. M. (2005). A COMPARISON OF SIX POTENTIAL EVAPOTRANSPIRATION METHODS FOR REGIONAL USE IN THE SOUTHEASTERN UNITED STATES. *Journal of the American Water Resources Association*, *41*(3), 621–633. https://doi.org/10.1111/j.1752-1688.2005.tb03759.x

Majozi, N., Mannaerts, C., Ramoelo, A., Mathieu, R., & Verhoef, W. (2021). Uncertainty and Sensitivity Analysis of a Remote-Sensing-Based Penman–Monteith Model to Meteorological and Land Surface Input Variables. *Remote Sensing*, *13*(5), 882. https://doi.org/10.3390/rs13050882

Mao, Y., & Wang, K. (2017). Comparison of evapotranspiration estimates based on the surface water balance, modified Penman-Monteith model, and reanalysis data sets for continental China: Terrestrial Evapotranspiration in China. *Journal of Geophysical Research: Atmospheres*, *122*(6), 3228–3244. https://doi.org/10.1002/2016JD026065

Massmann, A., Gentine, P., & Lin, C. (2019). When Does Vapor Pressure Deficit Drive or Reduce Evapotranspiration? *Journal of Advances in Modeling Earth Systems*, *11*(10), 3305–3320. https://doi.org/10.1029/2019MS001790

McGlynn, B. L., McDonnell, J. J., Seibert, J., & Kendall, C. (2004). Scale effects on headwater catchment runoff timing, flow sources, and groundwater-streamflow relations: SCALE EFFECTS ON CATCHMENT RUNOFF. *Water Resources Research*, *40*(7). https://doi.org/10.1029/2003WR002494

McMahon, G., Bales, J. D., Coles, J. F., Giddings, E. M. P., & Zappia, H. (2003). USE OF STAGE DATA TO CHARACTERIZE HYDROLOGIC CONDITIONS IN AN URBANIZING ENVIRONMENT1. *JOURNAL OF THE AMERICAN WATER RESOURCES ASSOCIATION*, 18.

Milesi, C., Hashimoto, H., Running, S. W., & Nemani, R. R. (2005). Climate variability, vegetation productivity and people at risk. *Global and Planetary Change*, *47*(2–4), 221–231. https://doi.org/10.1016/j.gloplacha.2004.10.020

Miller, J. (1990). *DEPARTMENT OF THE INTERIOR*. 30.

Miller, J. D., Kim, H., Kjeldsen, T. R., Packman, J., Grebby, S., & Dearden, R. (2014). Assessing the impact of urbanization on storm runoff in a peri-urban catchment using historical change in impervious cover. *Journal of Hydrology*, *515*, 59–70. https://doi.org/10.1016/j.jhydrol.2014.04.011

Mitchell, V. G., Cleugh, H. A., Grimmond, C. S. B., & Xu, J. (2008). Linking urban water balance and energy balance models to analyse urban design options. *Hydrological Processes*, *22*(16), 2891–2900. https://doi.org/10.1002/hyp.6868

Monteith, J. L. (1965). Evaporation and environment. *Symposia of the Society for Experimental Biology*, *19*, 205–234.

Myneni, R., Knyazikhin, Y., & Park, T. (2015). *MOD15A2H MODIS/Terra Leaf Area Index/FPAR 8-Day L4 Global 500m SIN Grid V006 [Data set]. Https://doi.org/10.5067/MODIS/MOD15A2H.006*. NASA EOSDIS Land Processes DAAC.

Oishi, A. C., Oren, R., Novick, K. A., Palmroth, S., & Katul, G. G. (2010). Interannual Invariability of Forest Evapotranspiration and Its Consequence to Water Flow Downstream. *Ecosystems*, *13*(3), 421–436. https://doi.org/10.1007/s10021-010-9328-3

Oke, T. R. (1979). Advectively-assisted evapotranspiration from irrigated urban vegetation. *Boundary-Layer Meteorology*, *17*(2), 167–173. https://doi.org/10.1007/BF00117976

Oke, T. R. (1981). Canyon geometry and the nocturnal urban heat island: Comparison of scale model and field observations. *Journal of Climatology*, *1*(3), 237–254. https://doi.org/10.1002/joc.3370010304

Penman, H. L., & Schofield, R. K. (1951). Some physical aspects of assimilation and transpiration. *Symposia of the Society for Experimental Biology*, *5*, 115–129.

Peters, E. B., Hiller, R. V., & McFadden, J. P. (2011). Seasonal contributions of vegetation types to suburban evapotranspiration. *Journal of Geophysical Research*, *116*(G1), G01003. https://doi.org/10.1029/2010JG001463

Ragab, R., Rosier, P., Dixon, A., Bromley, J., & Cooper, J. D. (2003). Experimental study of water fluxes in a residential area: 2. Road infiltration, runoff and evaporation. *Hydrological Processes*, *17*(12), 2423–2437. https://doi.org/10.1002/hyp.1251

Ramier, D., Berthier, E., & Andrieu, H. (2011). The hydrological behaviour of urban streets: Long-term observations and modelling of runoff losses and rainfall-runoff transformation. *Hydrological Processes*, *25*(14), 2161–2178. https://doi.org/10.1002/hyp.7968

Raoufi, R., & Beighley, E. (2017). Estimating Daily Global Evapotranspiration Using Penman–Monteith Equation and Remotely Sensed Land Surface Temperature. *Remote Sensing*, *9*(11), 1138. https://doi.org/10.3390/rs9111138

Raupach, M. R. (2001). Combination theory and equilibrium evaporation. *Quarterly Journal of the Royal Meteorological Society*, *127*(574), 1149–1181. https://doi.org/10.1002/qj.49712757402

S. Irmak & D. Mutiibwa. (2009). On the Dynamics of Stomatal Resistance: Relationships between Stomatal Behavior and Micrometeorological Variables and Performance of Jarvis-Type Parameterization. *Transactions of the ASABE*, *52*(6), 1923–1939. https://doi.org/10.13031/2013.29219

Safeeq, M., Bart, R. R., Pelak, N. F., Singh, C. K., Dralle, D. N., Hartsough, P., & Wagenbrenner, J. W. (2021). How realistic are water-balance closure assumptions? A demonstration from the southern sierra critical zone observatory and kings river experimental watersheds. *Hydrological Processes*, *35*(5). https://doi.org/10.1002/hyp.14199

Sailor, D. J., Georgescu, M., Milne, J. M., & Hart, M. A. (2015). Development of a national anthropogenic heating database with an extrapolation for international cities. *Atmospheric Environment*, *118*, 7–18. https://doi.org/10.1016/j.atmosenv.2015.07.016

Sailor, D. J., & Vasireddy, C. (2006). Correcting aggregate energy consumption data to account for variability in local weather. *Environmental Modelling & Software*, *21*(5), 733–738. https://doi.org/10.1016/j.envsoft.2005.08.001

Sanford, W. E., & Selnick, D. L. (2013). Estimation of Evapotranspiration Across the Conterminous United States Using a Regression With Climate and Land-Cover Data [1]. *JAWRA Journal of the American Water Resources Association*, *49*(1), 217–230. https://doi.org/10.1111/jawr.12010

Scott, R. L. (2010). Using watershed water balance to evaluate the accuracy of eddy covariance evaporation measurements for three semiarid ecosystems. *Agricultural and Forest Meteorology*, *150*(2), 219–225. https://doi.org/10.1016/j.agrformet.2009.11.002

Shuttleworth, W. J. (1978). A simplified one-dimensional theoretical description of the vegetation-atmosphere interaction. *Boundary-Layer Meteorology*, *14*(1), 3–27. https://doi.org/10.1007/BF00123986

Shuttleworth, W. J. (2007). Putting the "vap" into evaporation. *Hydrology and Earth System Sciences*, *11*(1), 210–244. https://doi.org/10.5194/hess-11-210-2007

Sloto, R., & Buxton. (2005). *Scientific Investigations Report* (Scientific Investigations Report) [Scientific Investigations Report].

Spera, A., & Richards, T. R. (1979). *MODIFIED POWER LAW EQUATIONS FOR VERTICAL WIND PROFILES*. 12.

Stathopoulou, M., Cartalis, C., & Petrakis, M. (2007). Integrating Corine Land Cover data and Landsat TM for surface emissivity definition: Application to the urban area of Athens, Greece. *International Journal of Remote Sensing*, *28*(15), 3291–3304. https://doi.org/10.1080/01431160600993421

Stewart, J. B. (1988). Modelling surface conductance of pine forest. *Agricultural and Forest Meteorology*, *43*(1), 19–35. https://doi.org/10.1016/0168-1923(88)90003-2

Stewart, J. B. (1989). *On the use of the Penrnan-Monteith equation for determining area! Évapotranspiration*. 10.

Sumner, D. M., & Jacobs, J. M. (2005). Utility of Penman–Monteith, Priestley–Taylor, reference evapotranspiration, and pan evaporation methods to estimate pasture evapotranspiration. *Journal of Hydrology*, *308*(1–4), 81–104. https://doi.org/10.1016/j.jhydrol.2004.10.023

Tan, C., Wong, N., Tan, P., Jusuf, S., & Chiam, Z. (2015). Impact of plant evapotranspiration rate and shrub albedo on temperature reduction in the tropical outdoor environment. *BUILDING AND ENVIRONMENT*, *94*, 206–217. https://doi.org/10.1016/j.buildenv.2015.08.001

Tan, J., Zheng, Y., Tang, X., Guo, C., Li, L., Song, G., Zhen, X., Yuan, D., Kalkstein, A. J., Li, F., & Chen, H. (2010). The urban heat island and its impact on heat waves and human health in Shanghai. *International Journal of Biometeorology*, *54*(1), 75–84. https://doi.org/10.1007/s00484-009-0256-x

Thompson, S. E., Harman, C. J., Konings, A. G., Sivapalan, M., Neal, A., & Troch, P. A. (2011). Comparative hydrology across AmeriFlux sites: The variable roles of climate, vegetation, and groundwater: POINT-SCALE MODELS AND VARIABLE CONTROLS ON ET. *Water Resources Research*, *47*(10). https://doi.org/10.1029/2010WR009797

Thornthwaite, C. W. (1948). *An Approach toward a Rational Classification of Climate*. 49.

Trlica, A., Hutyra, L. R., Schaaf, C. L., Erb, A., & Wang, J. A. (2017). Albedo, Land Cover, and Daytime Surface Temperature Variation Across an Urbanized Landscape: ALBEDO OF URBAN LANDSCAPE. *Earth's Future*, *5*(11), 1084–1101. https://doi.org/10.1002/2017EF000569

Vörösmarty, C. J., Federer, C. A., & Schloss, A. L. (1998). Potential evaporation functions compared on US watersheds: Possible implications for global-scale water balance and terrestrial ecosystem modeling. *Journal of Hydrology*, *207*(3–4), 147–169. https://doi.org/10.1016/S0022-1694(98)00109-7

Wang, J., Endreny, T. A., & Nowak, D. J. (2008). Mechanistic Simulation of Tree Effects in an Urban Water Balance Model [1]. *JAWRA Journal of the American Water Resources Association*, *44*(1), 75–85. https://doi.org/10.1111/j.1752-1688.2007.00139.x

Wang, Q., Xu, Y., Wang, Y., Zhang, Y., Xiang, J., Xu, Y., & Wang, J. (2020). Individual and combined impacts of future land-use and climate conditions on extreme hydrological events in a representative basin of the Yangtze River Delta, China. *Atmospheric Research*, *236*, 104805. https://doi.org/10.1016/j.atmosres.2019.104805

Williams, C. A., Reichstein, M., Buchmann, N., Baldocchi, D., Beer, C., Schwalm, C., Wohlfahrt, G., Hasler, N., Bernhofer, C., Foken, T., Papale, D., Schymanski, S., & Schaefer, K. (2012). Climate and vegetation controls on the surface water balance: Synthesis of evapotranspiration measured across a global network of flux towers: CLIMATE AND VEGETATION CONTROLS ON SURFACE WATER BALANCE. *Water Resources Research*, *48*(6). https://doi.org/10.1029/2011WR011586

Xia, J., Yan, Z., & Wu, P. (2013). Multidecadal variability in local growing season during 1901–2009. *Climate Dynamics*, *41*(2), 295–305. https://doi.org/10.1007/s00382-012-1438-5

Xie, X., Huang, Z., & Wang, J. (2005). Impact of building configuration on air quality in street canyon. *Atmospheric Environment*, *39*(25), 4519–4530. https://doi.org/10.1016/j.atmosenv.2005.03.043

Yuan, F., & Bauer, M. E. (2007). Comparison of impervious surface area and normalized difference vegetation index as indicators of surface urban heat island effects in Landsat imagery. *Remote Sensing of Environment*, *106*(3), 375–386. https://doi.org/10.1016/j.rse.2006.09.003

Yuan, M., Leirvik, T., & Wild, M. (2021). Global trends in downward surface solar radiation from spatial interpolated ground observations during 1961-2019. *Journal of Climate*, 1–56. https://doi.org/10.1175/JCLI-D-21-0165.1

Zhang, L., Dawes, W. R., & Walker, G. R. (2001). Response of mean annual evapotranspiration to vegetation changes at catchment scale. *Water Resources Research*, *37*(3), 701–708. https://doi.org/10.1029/2000WR900325

Zhou, J., Liu, J., Chu, Q., Wang, H., Shao, W., Luo, Z., & Zhang, Y. (2021). Mechanisms and Empirical Modeling of Evaporation from Hardened Surfaces in Urban Areas.

International Journal of Environmental Research and Public Health, *18*(4), 1790. https://doi.org/10.3390/ijerph180417

APPENDICES

Appendix A: NLCD Developed Classes Land Cover Data Collection

LC 21: Developed Open Space (Legend Below)

1		
2	1	1
2	1	1
2	1	1

2		
1	1	1
1	1	1
1	1	1

3		
4	4	4
1	1	1
2	2	2

4		
3	3	2
1	3	2
2	2	2

5		
1	1	1
1	1	1
1	1	1

6		
5	5	5
5	5	5
1	1	1

7		
1	1	1
1	1	1
1	1	1

8		
3	3	3
3	3	3
3	3	3

9		
1	1	1
1	1	1
1	1	1

10		
1	1	1
1	1	1
1	1	1

11		
1	1	1
1	1	1
1	1	1

12		
6	6	1
6	6	6
6	6	6

13		
1	3	4
1	1	1
1	1	1

14		
3	3	3
3	3	3
2	2	2

15		
2	2	2
3	3	3
1	1	1

16		
1	1	1
1	1	1
1	1	1

17		
1	3	3
1	1	1
1	1	1

18		
3	7	1
1	3	3
1	3	3

19		
1	1	1
1	1	3
3	1	1

20		
3	3	3
3	3	3
3	3	3

21		
3	3	2
3	3	2
1	3	2

22		
4	4	4
2	3	2
2	2	2

23		
3	3	3
3	3	3
3	3	3

24		
3	3	3
3	3	3
3	3	3

25		
2	2	1
2	3	1
2	3	3

26		
3	1	1
2	3	1
3	2	2

27		
1	1	1
1	1	1
1	1	1

28		
3	2	1
3	2	1
3	2	1

29		
3	2	3
3	2	3
2	2	2

30		
1	1	1
1	1	1
4	1	1

LEGEND	
Ref #	Landcover
1	Hardwood/pine forest
2	Paved roads
3	Grass
4	Structural Buildings
5	Golf course
6	Open water
7	Pool

Landcover	Count	Percent Cover
1	130	48.1
2	40	14.8
3	77	28.5
4	8	3.0
5	6	2.2
6	8	3.0
7	1	0.4
Total	270	

LC 22: Low-Intensity Developed

1		
3	4	3
1	1	1
1	1	1

2		
1	2	2
1	2	1
1	2	2

3		
1	1	1
3	1	1
3	1	1

4		
3	3	3
2	2	2
3	3	3

5		
3	3	3
3	3	3
4	3	3

6		
3	3	3
1	1	1
1	1	1

7		
3	3	1
3	3	4
3	3	4

8		
2	2	3
3	3	3
3	3	3

9		
3	3	3
3	3	3
3	3	3

10		
3	3	3
3	4	3
3	4	1

11		
1	3	3
1	3	4
1	3	4

12		
2	1	3
3	1	1
3	1	1

13		
2	2	3
2	3	3
2	3	4

14		
3	2	3
2	3	3
2	3	3

15		
2	3	3
2	2	3
3	3	3

16		
1	1	1
1	1	1
1	1	1

17		
1	1	3
2	2	2
3	1	1

18		
1	2	2
2	4	3
4	4	3

19		
2	2	2
3	4	4
3	3	4

20		
2	3	4
2	3	3
2	4	3

21		
1	1	4
3	1	1
3	4	1

22		
4	1	1
3	1	1
3	4	4

23		
4	4	3
3	4	4
3	3	3

24		
3	3	2
3	3	2
4	2	3

25		
1	1	3
1	1	3
1	1	3

26		
1	2	1
2	2	2
4	4	2

27		
3	3	4
3	3	4
2	3	4

28		
4	4	4
3	3	3
2	2	2

29		
3	3	2
4	3	2
3	3	2

30		
3	4	1
3	4	1
3	4	2

Code	Count	Percent
1	66	24.44
2	49	18.15
3	116	42.96
4	39	14.44

LC 23: Medium-Intensity Developed

1		
2	2	3
2	2	3
2	2	1

2		
3	3	3
2	2	2
2	2	2

3		
3	2	3
3	2	2
2	2	2

4		
3	3	3
2	3	3
2	3	3

5		
2	3	2
2	3	3
2	3	2

6		
2	1	1
2	1	1
2	1	1

7		
2	3	4
2	3	4
2	4	4

8		
3	2	2
1	1	2
1	2	3

9		
2	2	2
1	1	1
1	1	1

10		
2	2	1
4	4	1
4	4	1

11		
2	4	4
2	4	4
2	4	4

12		
4	4	2
4	4	2
4	4	2

13		
3	4	4
2	3	3
2	2	2

14		
2	2	2
3	2	2
1	3	2

15		
2	2	2
2	2	2
3	2	2

16		
2	2	2
2	2	2
2	2	2

17		
2	2	2
2	2	2
4	2	2

18		
2	2	1
2	2	2
2	2	2

19		
1	2	2
2	1	4
2	2	1

20		
2	2	2
3	3	3
3	3	3

21		
2	4	2
1	2	2
1	1	1

22		
1	1	1
2	2	1
2	2	2

23		
4	2	1
4	2	2
3	2	2

24		
4	2	2
4	3	2
4	3	2

25		
3	2	3
3	3	2
3	3	2

26		
2	3	3
2	2	2
1	1	1

27		
3	3	2
3	3	2
3	3	2

28		
3	4	3
4	4	3
1	3	4

29		
2	2	3
2	2	2
3	2	2

30		
2	2	2
3	2	2
2	2	2

Code	Count	%
1	36	13.33
2	142	52.59
3	58	21.48
4	34	12.59

LC 24: High Intensity Developed

1		
3	3	3
3	3	3
3	3	3

2		
2	2	2
2	2	2
2	2	2

3		
4	4	4
4	4	4
4	4	4

4		
2	2	2
2	2	2
2	2	2

5		
4	4	4
4	4	4
4	4	4

6		
1	1	1
1	1	1
1	1	1

7		
2	2	2
2	2	2
2	2	2

8		
2	2	2
2	2	2
1	2	2

9		
4	4	4
2	2	2
2	2	2

10		
2	2	2
2	2	2
4	4	4

11		
2	2	2
2	2	2
2	2	2

12		
3	2	2
2	2	2
4	2	2

13		
8	8	8
8	8	8
3	3	3

14		
2	2	2
2	2	2
2	2	2

15		
2	2	2
2	2	2
4	4	4

16		
2	2	2
2	2	2
2	2	2

17		
2	2	2
2	2	2
2	2	2

18		
2	2	2
4	4	4
4	4	4

19		
2	2	2
2	2	2
2	2	2

20		
2	4	4
2	2	2
2	2	2

21		
4	4	4
4	4	4
4	4	4

22		
2	2	2
2	2	2
2	2	2

23		
4	4	4
4	4	4
4	4	4

24		
2	2	2
2	2	2
2	2	4

25		
3	3	2
3	3	2
2	3	3

26		
2	2	2
2	2	2
2	2	2

27		
4	2	2
3	2	2
3	2	2

28		
4	2	2
2	2	2
2	2	2

29		
4	2	2
2	2	1
2	2	1

30		
3	2	2
4	2	2
4	4	3

Code	Count	%
1	12	4.44
2	178	65.93
3	19	7.04
4	61	22.59

Appendix B: NLCD Undeveloped Classes Land Cover Data Collection

Codes	Undeveloped LC Class									
Point	11	31	41	42	43	52	71	81	90	95
1	6	4	1	3	1	8	1	12	15	16
2	1	10	1	3	1	11	11	9	15	11
3	2	1	1	1	1	1	3	12	15	16
4	6	9	1	1	1	1	11	8	15	16
5	6	9	1	1	1	1	1	11	15	3
6	6	2	1	1	1	3	8	14	15	11
7	2	9	1	1	3	2	2	3	15	16
8	2	2	3	1	3	3	1	3	15	16
9	6	3	1	1	1	3	11	12	1	3

10	6	3	3	1	3	1	1	1	1	16
11	6	2	1	1	1	3	1	3	15	16
12	1	3	1	1	1	11	1	12	15	16
13	6	10	1	1	1	3	1	12	1	16
14	6	9	3	1	1	11	11	3	15	11
15	1	3	3	3	1	1	11	12	15	16
16	6	9	1	1	1	1	11	1	15	15
17	6	9	1	1	1	11	4	12	1	15
18	6	10	1	1	1	1	10	9	1	3
19	6	3	1	1	1	1	11	3	15	16
20	16	10	1	1	7	1	2	1	15	16
21	1	8	1	1	1	1	1	3	1	16
22	6	3	1	1	1	3	1	2	15	16
23	1	8	3	1	1	11	4	3	15	16
24	16	9	1	1	1	1	11	12	15	16
25	6	9	1	1	1	11	1	12	15	16
26	6	1	1	1	2	11	8	12	1	16
27	6	10	1	1	3	3	1	9	15	16
28	6	2	3	3	1	1	8	1	15	16
29	6	2	3	1	3	1	2	12	15	15
30	6	10	1	1	3	1	3	4	15	16
31	6	10	1	1	1	11	3	3	1	6
32	6	10	1	1	1	11	1	3	15	16
33	6	10	1	1	1	11	8	3	1	3
34	6	10	1	1	1	3	8	3	15	16
35	6	10	1	1	1	3	8	3	15	6
36	6	9	1	1	1	1	8	3	15	16
37	6	2	1	1	1	11	8	3	15	16
38	6	1	1	1	1	1	10	3	1	6
39	6	9	1	1	1	11	1	1	1	3
40	6	9	1	1	1	1	3	3	1	16
41	1	9	1	1	8	1	3	3	1	16
42	6	11	1	1	1	3	3	3	15	3
43	6	11	1	1	1	3	3	3	15	16
44	6	2	1	1	1	1	2	3	15	6
45	6	9	1	1	1	1	3	3	15	8
46	6	11	1	1	1	11	8	3	15	16
47	6	3	1	1	1	11	8	3	15	2
48	6	10	1	1	1	11	8	3	1	16
49	6	10	1	1	1	3	8	3	1	1
50	6	9	1	1	1	8	11	3	15	16

Counts	NLCD LC Class													
	11	21	22	23	24	31	41	42	43	52	71	81	90	95
Forest	6	130	66	36	12	3	43	46	41	20	13	5	15	1
Paved Roads	3	40	49	142	178	7	0	0	1	1	4	1	0	1
Grass	0	77	116	58	19	7	7	4	6	12	8	26	0	6
Built Structure	0	8	39	34	61	1	0	0	0	0	2	1	0	0
Golf Course	0	6	0	0	0	0	0	0	0	0	0	0	0	0
Open Water	39	8	0	0	0	0	0	0	0	0	0	0	0	4
Pool	0	1	0	0	0	0	0	0	1	0	0	0	0	0
Bare Soil	0	0	0	0	0	2	0	0	1	2	12	1	0	1
Landfill	0	0	0	0	0	14	0	0	0	0	0	3	0	0
Exposed Rock	0	0	0	0	0	13	0	0	0	0	2	0	0	0
Short Vegetation	0	0	0	0	0	3	0	0	0	15	9	1	0	3
Pasture/Hay	0	0	0	0	0	0	0	0	0	0	0	11	0	0
Crops	0	0	0	0	0	0	0	0	0	0	0	0	0	0
Cemetery	0	0	0	0	0	0	0	0	0	0	0	1	0	0
Woody Wetland	0	0	0	0	0	0	0	0	0	0	0	0	35	3
Herbaceous Wetland	2	0	0	0	0	0	0	0	0	0	0	0	0	31

Percentages	NLCD LC Class													
	11	21	22	23	24	31	41	42	43	52	71	81	90	95
Forest	0.12	0.48	0.24	0.13	0.04	0.06	0.86	0.92	0.82	0.40	0.26	0.10	0.30	0.02
Paved Roads	0.06	0.15	0.18	0.53	0.66	0.14	0	0	0.02	0.02	0.08	0.02	0	0.02
Grass	0	0.29	0.43	0.21	0.07	0.14	0.14	0.08	0.12	0.24	0.16	0.52	0	0.12
Built Structure	0	0.03	0.14	0.13	0.23	0.02	0	0	0	0	0.04	0.02	0	0
Golf Course	0	0.02	0	0	0	0	0	0	0	0	0	0	0	0
Open Water	0.78	0.03	0	0	0	0	0	0	0	0	0	0	0	0.08
Pool	0	0.004	0	0	0	0	0	0	0.02	0	0	0	0	0
Bare Soil	0	0	0	0	0	0.04	0	0	0.02	0.04	0.24	0.02	0	0.02
Landfill	0	0	0	0	0	0.28	0	0	0	0	0	0.06	0	0
Exposed Rock	0	0	0	0	0	0.26	0	0	0	0	0.04	0	0	0
Short Vegetation	0	0	0	0	0	0.06	0	0	0	0.30	0.18	0.02	0	0.06
Pasture/Hay	0	0	0	0	0	0	0	0	0	0	0	0.22	0	0
Cemetery	0	0	0	0	0	0	0	0	0	0	0	0.02	0	0
Woody Wetland	0	0	0	0	0	0	0	0	0	0	0	0	0.70	0.06
Herbaceous Wetland	0.04	0	0	0	0	0	0	0	0	0	0	0	0	0.62

Appendix C: Areas of NLCD Classes after Interpolation Procedure 2001-2020

Pixels															
Year	LC11	LC21	LC22	LC23	LC24	LC31	LC41	LC42	LC43	LC52	LC71	LC81	LC90	LC95	Sum
2001	2553.7	134975	123917	54382	35460	1249.9	67698	59014	19310	1618.8	7669.1	14003	8450	109.16	530409
2002	2538.9	134997	124194	55041	35705	1232.2	67379	58685	19313	1614.2	7446.6	13771	8453.1	118	530488
2003	2524.1	135020	124472	55700	35950	1214.5	67059	58357	19315	1609.7	7224.2	13539	8456.2	126.85	530566
2004	2509.3	135042	124749	56359	36195	1196.8	66739	58029	19318	1605.1	7001.7	13307	8459.3	135.69	530645
2005	2494.5	135065	125027	57017	36439	1179.1	66420	57701	19320	1600.6	6779.2	13075	8462.4	144.53	530724
2006	2479.7	135087	125304	57676	36684	1161.4	66100	57373	19323	1596	6556.7	12843	8465.5	153.37	530803
2007	2464.9	135110	125581	58335	36929	1143.6	65780	57045	19326	1591.5	6334.2	12611	8468.6	162.21	530881
2008	2450.1	135132	125859	58994	37174	1125.9	65461	56716	19328	1587	6111.7	12379	8471.7	171.05	530960
2009	2435.3	135154	126136	59652	37419	1108.2	65141	56388	19331	1582.4	5889.3	12147	8474.8	179.9	531039
2010	2420.5	135177	126413	60311	37664	1090.5	64821	56060	19333	1577.9	5666.8	11915	8477.9	188.74	531118
2011	2405.7	135199	126691	60970	37909	1072.8	64502	55732	19336	1573.3	5444.3	11684	8481	197.58	531197
2012	2390.9	135222	126968	61629	38154	1055.1	64182	55404	19339	1568.8	5221.8	11452	8484.1	206.42	531275
2013	2376.1	135244	127245	62287	38399	1037.4	63862	55076	19341	1564.2	4999.3	11220	8487.2	215.26	531354
2014	2361.3	135267	127523	62946	38644	1019.6	63543	54747	19344	1559.7	4776.9	10988	8490.3	224.1	531433
2015	2346.5	135289	127800	63605	38889	1001.9	63223	54419	19346	1555.1	4554.4	10756	8493.4	232.95	531512
2016	2331.7	135312	128078	64264	39134	984.21	62904	54091	19349	1550.6	4331.9	10524	8496.5	241.79	531590
2017	2316.9	135334	128355	64922	39378	966.5	62584	53763	19352	1546.1	4109.4	10292	8499.6	250.63	531669
2018	2302.1	135357	128632	65581	39623	948.79	62264	53435	19354	1541.5	3886.9	10060	8502.7	259.47	531748
2019	2287.3	135379	128910	66240	39868	931.07	61945	53107	19357	1537	3664.4	9828.1	8505.8	268.31	531827
2020	2272.5	135402	129187	66899	40113	913.36	61625	52778	19359	1532.4	3442	9596.2	8508.9	277.15	531905

Pixels Proportion														
Year	LC11	LC21	LC22	LC23	LC24	LC31	LC41	LC42	LC43	LC52	LC71	LC81	LC90	LC95
2001	0.0048	0.2545	0.2336	0.1025	0.0669	0.0024	0.1276	0.1113	0.0364	0.0031	0.0145	0.0264	0.0159	0.0002
2002	0.0048	0.2545	0.2341	0.1038	0.0673	0.0023	0.127	0.1106	0.0364	0.003	0.014	0.026	0.0159	0.0002
2003	0.0048	0.2545	0.2346	0.105	0.0678	0.0023	0.1264	0.11	0.0364	0.003	0.0136	0.0255	0.0159	0.0002
2004	0.0047	0.2545	0.2351	0.1062	0.0682	0.0023	0.1258	0.1094	0.0364	0.003	0.0132	0.0251	0.0159	0.0003
2005	0.0047	0.2545	0.2356	0.1074	0.0687	0.0022	0.1251	0.1087	0.0364	0.003	0.0128	0.0246	0.0159	0.0003
2006	0.0047	0.2545	0.2361	0.1087	0.0691	0.0022	0.1245	0.1081	0.0364	0.003	0.0124	0.0242	0.0159	0.0003
2007	0.0046	0.2545	0.2366	0.1099	0.0696	0.0022	0.1239	0.1075	0.0364	0.003	0.0119	0.0238	0.016	0.0003
2008	0.0046	0.2545	0.237	0.1111	0.07	0.0021	0.1233	0.1068	0.0364	0.003	0.0115	0.0233	0.016	0.0003
2009	0.0046	0.2545	0.2375	0.1123	0.0705	0.0021	0.1227	0.1062	0.0364	0.003	0.0111	0.0229	0.016	0.0003
2010	0.0046	0.2545	0.238	0.1136	0.0709	0.0021	0.122	0.1056	0.0364	0.003	0.0107	0.0224	0.016	0.0004
2011	0.0045	0.2545	0.2385	0.1148	0.0714	0.002	0.1214	0.1049	0.0364	0.003	0.0102	0.022	0.016	0.0004
2012	0.0045	0.2545	0.239	0.116	0.0718	0.002	0.1208	0.1043	0.0364	0.003	0.0098	0.0216	0.016	0.0004
2013	0.0045	0.2545	0.2395	0.1172	0.0723	0.002	0.1202	0.1037	0.0364	0.0029	0.0094	0.0211	0.016	0.0004
2014	0.0044	0.2545	0.24	0.1184	0.0727	0.0019	0.1196	0.103	0.0364	0.0029	0.009	0.0207	0.016	0.0004
2015	0.0044	0.2545	0.2404	0.1197	0.0732	0.0019	0.1189	0.1024	0.0364	0.0029	0.0086	0.0202	0.016	0.0004
2016	0.0044	0.2545	0.2409	0.1209	0.0736	0.0019	0.1183	0.1018	0.0364	0.0029	0.0081	0.0198	0.016	0.0005
2017	0.0044	0.2545	0.2414	0.1221	0.0741	0.0018	0.1177	0.1011	0.0364	0.0029	0.0077	0.0194	0.016	0.0005
2018	0.0043	0.2546	0.2419	0.1233	0.0745	0.0018	0.1171	0.1005	0.0364	0.0029	0.0073	0.0189	0.016	0.0005
2019	0.0043	0.2546	0.2424	0.1246	0.075	0.0018	0.1165	0.0999	0.0364	0.0029	0.0069	0.0185	0.016	0.0005
2020	0.0043	0.2546	0.2429	0.1258	0.0754	0.0017	0.1159	0.0992	0.0364	0.0029	0.0065	0.018	0.016	0.0005

Area (km2)														
Year	LC11	LC21	LC22	LC23	LC24	LC31	LC41	LC42	LC43	LC52	LC71	LC81	LC90	LC95
2001	2.2961	121.36	111.42	48.896	31.882	1.1238	60.868	53.06	17.362	1.4555	6.8954	12.59	7.5975	0.0981
2002	2.2825	121.36	111.65	49.481	32.098	1.1077	60.572	52.757	17.362	1.4512	6.6944	12.38	7.5992	0.1061
2003	2.2688	121.36	111.88	50.066	32.313	1.0917	60.276	52.454	17.361	1.4469	6.4934	12.169	7.6008	0.114
2004	2.2552	121.36	112.11	50.65	32.529	1.0756	59.98	52.152	17.361	1.4426	6.2925	11.959	7.6025	0.1219
2005	2.2415	121.37	112.35	51.235	32.744	1.0595	59.683	51.849	17.361	1.4383	6.0917	11.749	7.6042	0.1299
2006	2.2279	121.37	112.58	51.819	32.959	1.0434	59.387	51.546	17.361	1.434	5.8909	11.539	7.6058	0.1378
2007	2.2143	121.37	112.81	52.403	33.174	1.0274	59.091	51.244	17.36	1.4297	5.6901	11.329	7.6075	0.1457
2008	2.2007	121.37	113.04	52.987	33.389	1.0113	58.796	50.942	17.36	1.4254	5.4895	11.119	7.6091	0.1536
2009	2.187	121.38	113.28	53.571	33.604	0.9952	58.5	50.639	17.36	1.4211	5.2888	10.909	7.6108	0.1616
2010	2.1734	121.38	113.51	54.154	33.819	0.9792	58.204	50.337	17.36	1.4168	5.0883	10.699	7.6124	0.1695
2011	2.1598	121.38	113.74	54.738	34.034	0.9631	57.909	50.035	17.36	1.4125	4.8878	10.489	7.6141	0.1774
2012	2.1462	121.38	113.97	55.321	34.249	0.9471	57.613	49.733	17.359	1.4082	4.6874	10.279	7.6157	0.1853
2013	2.1326	121.38	114.2	55.904	34.463	0.931	57.318	49.431	17.359	1.4039	4.487	10.07	7.6174	0.1932
2014	2.119	121.39	114.44	56.487	34.678	0.915	57.022	49.129	17.359	1.3996	4.2867	9.8602	7.619	0.2011
2015	2.1054	121.39	114.67	57.069	34.893	0.899	56.727	48.828	17.359	1.3954	4.0864	9.6506	7.6207	0.209
2016	2.0918	121.39	114.9	57.652	35.107	0.883	56.432	48.526	17.358	1.3911	3.8862	9.4412	7.6224	0.2169
2017	2.0782	121.39	115.13	58.234	35.322	0.8669	56.137	48.224	17.358	1.3868	3.6861	9.2317	7.624	0.2248
2018	2.0646	121.39	115.36	58.816	35.536	0.8509	55.842	47.923	17.358	1.3825	3.486	9.0224	7.6257	0.2327
2019	2.051	121.4	115.6	59.398	35.751	0.8349	55.547	47.622	17.358	1.3782	3.286	8.813	7.6273	0.2406
2020	2.0375	121.4	115.83	59.98	35.965	0.8189	55.252	47.32	17.357	1.3739	3.086	8.6038	7.629	0.2485

Appendix D: Observed Heights of Buildings and Vegetation in NLCD Classes

		Building Heights (m)			
		Developed Open Space (21)	Low Intensity Developed (22)	Medium Intensity Developed (23)	High Intensity Developed (24)
Points	1	4.86	6.27	14.35	4.86
	2	7.48	10.4	6.02	5.54
	3	8.91	9.69	11.99	7.1
	4	7.14	11.05	9.03	5.65
	5	9.58	13.13	8.29	15.24
	6	8.52	10.59	11.69	4.41
	7	8.95	8.71	10.98	7.08
	8	6.03	8.86	10.22	9.2
	9	10.44	11.63	30.21	11.04
	10	8.02	8.75	4.47	15.74
	11	7.92	6.28	5.23	8.95
	12	10.89	9.86	9.15	13.2
	13	9.47	15.2	7.81	6.87
	14	12.57	6.77	5.83	8.25
	15	10.5	4.84	6.03	5.23
	16	8.2	10.06	22.99	12.47
	17	7.25	11.7	7.25	9.41
	18	9.52	10.99	61.85	8.3
	19	8.38	8.2	6.93	13.85
	20	7.04	10.69	7.38	4.11
	21	9.39	6.57	5.27	6.4
	22	6.71	7.49	17.69	27.6
	23	11.21	7.89	5.08	13.07
	24	13.25	4.6	7.82	5.47
	25	5.35	9.47	6.53	14.01
	26	9.38	10.48	7.62	10.93
	27	6.77	8.2	5.4	7.19
	28	11.29	8.21	8.46	8.41
	29	8.23	5.51	7.89	8.17
	30	7.51	4.94	10.85	31.26
	Average	8.69	8.90	11.34	10.30

		Vegetation Height (m)					
		Deciduous Forest (41)	Coniferous Forest (42)	Mixed Forest (43)	Shurb/Scrub (52)	Pasture/Grassland (71,81)*	Vegetated Wetlands (90,95)
Points	1	26.21	24.99	23.77	3.96	0.12	8.45
	2	23.47	21.95	22.25	17.07	0.12	9.95
	3	33.83	32.00	21.03	7.01	0.12	10.47
	4	18.98	27.74	22.86	0.91	0.12	4.06
	5	26.21	36.27	21.34	2.44	0.12	3.78
	6	22.25	26.82	16.15	6.71	0.12	11.51
	7	22.56	27.74	24.38	4.88	0.12	7.79
	8	23.77	22.56	23.47	4.57	0.12	12.88
	9	19.51	32.61	29.87	2.74	0.12	12.26
	10	21.34	27.74	22.86	1.22	0.12	8.86
	11	29.57	29.57	24.69	5.79	0.12	13.74
	12	25.30	18.90	17.68	7.32	0.12	4.08
	13	28.35	26.21	23.77	4.27	0.12	8.27
	14	26.21	22.25	19.20	2.74	0.12	7.84
	15	28.96	31.39	32.00	4.57	0.12	10.49
	16	21.34	26.52	22.56	2.13	0.12	11.35
	17	21.34	24.38	15.85	1.83	0.12	12.02
	18	15.54	28.65	16.76	3.66	0.12	4.79
	19	17.37	23.77	10.67	3.66	0.12	8.3
	20	19.51	29.57	25.60	1.22	0.12	8.24
	21	27.43	34.14	31.09	7.32	0.12	5.64
	22	24.38	26.21	31.09	1.22	0.12	10.17
	23	26.52	32.31	27.13	3.35	0.12	13.14
	24	23.77	26.21	16.15	0.91	0.12	9.34
	25	17.07	22.86	27.74	4.27	0.12	8.88
	26	20.73	33.22	24.08	2.13	0.12	4.06
	27	23.47	37.49	24.08	3.05	0.12	6.02
	28	31.09	23.47	24.69	2.74	0.12	11.42
	29	31.39	34.14	28.35	5.18	0.12	10.73
	30	23.77	19.51	23.47	0.91	0.12	6.8
	Average	24.04	27.71	23.15	3.99	0.12	8.84

Appendix E: NLCD Developed Class Composition 95% Confidence Intervals

			NLCD LC Class			
			Developed Open Space (21)	Low Intensity Developed (22)	Medium Intensity Developed (23)	High Intensity Developed (24)
Actual Land Cover Composition	Forest	Lower Bound	32.88	13.26	5.75	0
		Average	48.15	24.44	13.33	4.44
		Upper Bound	63.41	35.63	20.91	11.39
	Grassland	Lower Bound	17.68	33.48	13.03	0.44
		Average	30.74	42.96	21.85	10.74
		Upper Bound	43.8	52.45	30.67	21.05
	Impervious	Lower Bound	8.49	24.69	55.77	72.76
		Average	17.78	33.7	64.44	84.82
		Upper Bound	27.06	42.7	73.12	96.68
	Open water	Lower Bound	0	0	0	0
		Average	3.33	0	0	0
		Upper Bound	9.41	0	0	0

Appendix F: All Models' Annual ET for All Watersheds

South River Watershed (SRW)

Year	TerraClimate	PM	Fang Type I	Fang Type I Lumped	Fang Type II	Fang Type II Lumped	Lu	Sanford & Selnick Climate Only	Sanford & Selnick Climate-and-LC
2001	948.48	835.12	769.95	554.78	660.84	845.05	714.68	764.51	750.37
2002	901.88	838.24	792.05	590.95	704.39	904.31	832.13	822.82	778.60
2003	1013.13	787.97	768.66	581.41	696.50	895.41	892.62	839.90	791.16
2004	971.16	806.12	773.46	582.81	694.66	892.63	809.89	815.32	774.12
2005	1051.99	798.66	769.51	577.97	688.54	886.87	802.99	815.68	776.37
2006	906.09	848.78	781.90	577.47	686.90	884.84	716.66	760.43	741.97
2007	783.48	838.86	771.25	572.84	673.74	867.82	615.83	632.98	649.93
2008	957.01	826.19	760.83	560.94	661.32	853.84	702.55	752.50	740.64
2009	1034.76	742.73	760.99	594.47	702.28	910.08	942.69	841.81	791.33
2010	987.61	807.75	775.49	592.57	698.30	904.24	716.58	766.17	749.47
2011	927.61	864.48	789.81	589.00	692.15	897.46	688.46	732.05	721.30
2012	954.69	836.41	776.38	591.16	693.97	896.38	668.85	702.88	694.98
2013	1047.50	781.28	755.72	579.09	679.25	883.63	879.92	835.31	785.75
2014	1043.34	794.93	752.53	569.68	666.18	867.56	771.27	813.56	783.62
2015	1091.37	776.91	792.64	632.18	742.33	966.93	928.74	811.74	756.61
2016	841.83	784.64	774.80	615.47	716.60	935.64	688.24	723.25	707.17
2017	1180.60	731.98	751.51	607.54	712.53	928.59	802.69	792.29	745.45
2018	1105.50	729.50	766.62	626.39	734.24	960.44	898.54	813.37	758.70
2019	1012.89	775.02	770.42	620.47	721.75	946.30	757.46	772.81	734.64
2020	1129.17	772.66	783.81	623.01	732.79	960.24	935.74	809.75	754.17
Average	994.50	798.91	771.92	592.01	697.96	904.41	788.33	780.96	749.32

Year	TerraClimate	PM	Fang Type I	Fang Type I Lumped	Fang Type II	Fang Type II Lumped	Lu	Sanford & Selnick Climate Only	Sanford & Selnick Climate-and-LC
2001	968.07	1351.94	1060.35	1098.14	782.82	823.39	834.23	785.20	806.76
2002	955.63	930.73	890.29	894.94	819.69	870.14	829.11	773.70	792.76
2003	1067.40	859.29	849.40	849.64	790.31	849.77	873.82	800.60	802.47
2004	988.73	919.27	884.39	886.73	809.60	858.80	874.77	809.47	813.51
2005	1102.05	883.30	870.49	870.37	803.18	853.77	899.05	823.53	821.34
2006	968.12	971.33	916.71	916.37	824.50	867.02	756.84	690.05	738.13
2007	873.55	973.25	922.80	934.10	831.20	859.58	795.41	746.54	781.48
2008	1039.67	961.44	896.45	904.17	792.54	833.55	865.94	808.50	816.40
2009	1092.23	882.71	864.67	871.47	793.04	856.47	1023.39	845.51	822.91
2010	1045.52	1008.94	939.99	954.45	843.27	883.32	906.03	828.43	824.24
2011	928.87	1055.67	962.07	967.77	843.74	881.71	814.63	772.16	800.38
2012	898.87	1007.22	939.88	952.83	847.23	878.57	770.85	711.54	751.73
2013	1089.26	883.92	864.17	868.76	777.40	836.44	937.23	821.87	805.12
2014	1081.08	955.30	895.26	904.24	787.20	836.85	840.29	780.00	790.59
2015	1086.98	908.48	908.70	918.72	855.19	913.59	943.11	848.79	836.38
2016	942.07	1009.60	968.05	974.96	883.00	918.89	770.83	717.48	760.28
2017	1186.90	909.86	910.33	912.83	845.20	894.32	873.14	820.91	826.08
2018	1186.90	865.14	905.26	900.44	853.86	911.98	958.32	848.98	832.63
2019	1025.11	975.81	958.83	955.18	875.36	918.83	840.52	799.37	816.06
2020	1142.37	894.49	902.62	896.56	843.15	907.84	958.32	850.18	833.61
Average	1033.47	960.38	915.54	921.63	825.07	872.74	868.29	794.14	803.64

Fausett Creek Watershed

Year	TerraClimate	PM	Fang Type I	Fang Type I Lumped	Fang Type II	Fang Type II Lumped	Lu	Sanford & Selnick Climate Only	Sanford & Selnick Climate-and-LC
2001	991.19	1219.29	975.94	1025.90	714.35	766.45	812.98	812.24	794.31
2002	943.74	887.49	839.06	862.74	761.71	813.70	837.01	819.96	797.60
2003	955.26	811.59	784.96	809.44	730.44	788.52	908.46	789.34	765.07
2004	990.69	847.29	814.66	837.91	750.81	805.04	857.92	800.29	771.87
2005	982.42	819.39	798.36	820.97	742.46	793.18	781.18	800.68	777.75
2006	971.10	867.79	824.94	848.60	749.85	797.76	711.86	828.10	807.12
2007	837.24	895.03	845.81	870.55	757.32	797.93	622.09	848.24	826.90
2008	960.34	834.77	796.95	824.58	725.17	774.58	749.87	812.53	785.01
2009	987.94	786.49	780.00	808.05	722.66	778.49	889.53	781.17	749.46
2010	961.87	858.68	827.97	852.83	752.96	800.41	694.55	788.43	760.34
2011	968.91	865.12	830.55	856.30	758.81	813.71	800.64	820.86	792.70
2012	1051.46	853.85	830.56	854.88	756.31	804.16	745.30	837.66	808.92
2013	973.16	777.14	766.36	797.75	712.28	776.20	994.16	766.45	732.07
2014	1027.05	798.75	775.01	806.72	704.97	755.88	752.62	798.70	768.03
2015	1067.38	838.54	840.70	865.84	775.98	834.46	912.63	819.52	787.61
2016	905.61	896.60	880.41	902.99	801.30	847.34	654.47	855.10	829.27
2017	1124.40	860.01	842.44	867.73	772.34	830.26	874.11	833.24	803.49
2018	1124.40	818.55	831.63	852.75	787.69	848.32	926.65	806.31	772.95
2019	1060.97	816.15	844.81	863.53	805.37	863.20	857.91	836.92	812.42
2020	1091.28	749.91	803.79	821.43	781.50	842.83	932.28	810.38	779.56
Average	998.82	855.12	826.75	852.57	753.21	806.62	815.81	813.31	786.12

Appendix G: Sensitivity Analysis Results

On the day with highest ET in entire study (J=168, June 17, 2001)

Mixed Forest

Variable	Time-step and source	Value used on sensitivity date	ET on that day (before surface water availability and areal weighting)	Low value to try (10%)	ET using low value	High value to try (10%)	ET using high value
Temperature (°C)	Daily mean	24.48	5.96	22.03	5.70	26.93	6.20
Albedo	Constant w/ LC	0.1295	5.96	0.1165	6.06	0.1425	5.86
Relative Humidity (%)	Daily mean	62.6	5.96	56.34	5.88	68.86	6.03
Incoming Solar Radiation (MJ/m^2)	Daily mean	30.44	5.96	27.40	5.36	33.48	6.57
30 m Wind Speed (m/s)	Daily mean	2.94	5.96	2.64	5.88	3.23	6.02
Feature Height (m)	Constant w/ LC	23.15	5.96	20.84	6.12	25.47	5.78

Grass

Variable	Time-step and source	Value used on sensitivity date	ET on that day (before surface water availability and areal weighting)	Low value to try	ET using low value	High value to try	ET using high value
Temperature (°C)	Daily mean	24.48	5.391	22.03	5.22	26.93	5.55
Albedo	Constant w LC	0.144	5.391	0.129	5.48	0.158	5.30
Relative Humidity (%)	Daily mean	62.6	5.391	56.34	5.38	68.86	5.40
Incoming Solar Radiation (MJ/m^2)	Daily mean	30.44	5.391	27.40	4.92	33.48	5.87
3 m Wind Speed (m/s)	Daily mean	1.393	5.391	1.253	5.3970	1.53	5.386
Feature Height (m)	Constant w LC	0.12	5.391	0.108	5.3978	0.132	5.3847

Low-Intensity Developed

Variable	Time-step and source	Value used on sensitivity date	ET on that day (before surface water availability and areal weighting)	Low value to try	ET using low value	High value to try	ET using high value
Temperature (°C)	Daily mean	24.48	2.49	22.03	2.41	26.93	2.54
Albedo	Constant w LC	0.18	2.49	0.162	2.54	0.198	2.44
Relative Humidity (%)	Daily mean	62.6	2.49	56.34	2.51	68.86	2.43
Incoming Solar Radiation (MJ/m^2)	Daily mean	30.44	2.49	27.40	2.29	33.48	2.69
10 m Wind Speed (m/s)	Daily mean	2.02	2.49	1.82	2.51	2.22	2.47
Feature Height (m)	Constant w LC	8.9	2.49	8.01	2.52	9.79	2.46

High-Intensity Developed

Variable	Time-step and source	Value used on sensitivity date	ET on that day (before surface water availability and areal weighting)	Low value to try	ET using low value	High value to try	ET using high value
Temperature (°C)	Daily mean	24.48	2.50	22.03	2.42	26.93	2.56
Albedo	Constant w LC	0.2	2.50	0.18	2.56	0.22	2.45
Relative Humidity (%)	Daily mean	62.6	2.50	56.34	2.52	68.86	2.46
Incoming Solar Radiation (MJ/m^2)	Daily mean	30.44	2.50	27.40	2.35	33.48	2.70
30 m Wind Speed (m/s)	Daily mean	2.94	2.50	2.64	2.52	3.23	2.49
Feature Height (m)	Constant w LC	10.3	2.50	9.27	2.53	11.33	2.48